

Holographic Non-Hermitian Lattices and Junctions with \mathcal{PT} -Restoring RG Flows

Daniel Areán,^{1,2} David Garcia-Fariña^{1,2}

¹*Instituto de Física Teórica UAM/CSIC, Calle Nicolás Cabrera 13-15, 28049 Madrid, Spain*

²*Departamento de Física Teórica, Universidad Autónoma de Madrid, Campus de Cantoblanco, 28049 Madrid, Spain*

E-mail: daniel.arean@uam.es,
david.garciafarinna@estudiante.uam.es

ABSTRACT: We construct and study inhomogeneous non-Hermitian strongly coupled holographic field theories. We consider two models: a lattice where in each site there is some inflow/outflow of matter and a Hermitian/non-Hermitian/Hermitian junction. Depending on whether we turn on a complex external gauge field, we find solutions that spontaneously break \mathcal{PT} (thus hinting at a lack of unitary evolution) and solutions that do not. The former present an imaginary current responsible for the spontaneous breaking of \mathcal{PT} . We also study the IR geometry of these solutions finding that they flow to a \mathcal{PT} -unbroken fixed point. This leads us to claim that there is a \mathcal{PT} -symmetry restoration in the IR, similar to the one observed in the perturbative setup of [1].

Contents

1	Introduction	1
2	Holographic Model	4
2.1	Non-Hermitian CFT	4
2.2	Dyson map as an external gauge transformation	6
2.3	Gravitational dual	7
2.4	Matching symmetries	9
3	Non-Hermitian lattice	10
3.1	Numerical method	11
3.2	Numerical solutions	11
3.2.1	\mathcal{PT} broken phase	11
3.2.2	\mathcal{PT} unbroken phase	14
3.3	Quasinormal frequencies and stability	16
3.4	Null energy condition	18
3.5	Low-temperature behaviour	22
3.5.1	The zero temperature solution	24
4	Non-Hermitian junction	27
5	Conclusions	30
A	Holographic dictionary	32
B	Further details on the computation of the QNFs	33
B.1	Toy model: Probe limit	34
B.2	Adding backreaction	37

1 Introduction

One of the main axioms of Quantum Mechanics is that the Hamiltonian should be Hermitian. Underlying this assumption lies the need for unitary evolution, which is equivalent to demanding real eigenvalues of the Hamiltonian. However, when considering unitarity as the true physical restriction, one finds that Quantum Mechanics can also be consistently formulated with non-Hermitian Hamiltonians [2]. These non-Hermitian theories are instead required to have \mathcal{PT} symmetry [2] or, more generally an antilinear symmetry as recently emphasized in [3]. However, the existence

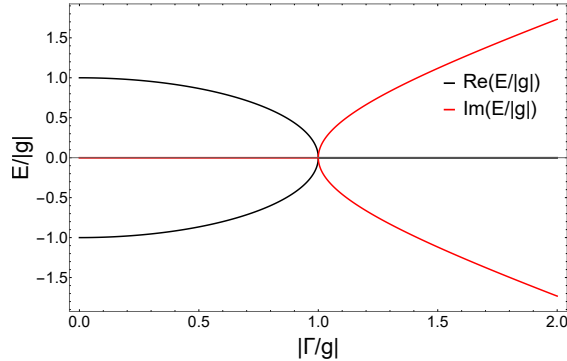


Figure 1: Energy levels in the two-level system (1.1). For $|\Gamma/g| > 1$ the energies become complex conjugate and \mathcal{PT} -symmetry is broken.

of such symmetry is not a sufficient condition for unitary evolution as it can be spontaneously broken by the spectrum of the theory. This realization gave rise to the field of \mathcal{PT} -symmetric Quantum Mechanics, and later to that of \mathcal{PT} -symmetric Quantum Field Theory (see, for instance, [4] for an introduction to these topics).

Physically, one thinks of a non-Hermitian theory as a theory with influx and outflux of matter. Within this perspective, it is clear that \mathcal{PT} -symmetric theories correspond to the family of non-Hermitian theories where influx and outflux are balanced, ensuring that matter content is conserved.

In practice, a \mathcal{PT} -symmetric theory can be mapped to a Hermitian one via a Dyson map [5–7]. Nonetheless, in many cases, the mapping can be highly non-trivial and give rise to non-local interactions. This alone motivates us to study non-Hermitian theories for their own physical relevance. Moreover, once we rid ourselves of the constraints of Hermiticity and instead construct \mathcal{PT} -symmetric Hamiltonians, we can begin to study the vacua and the spontaneous breaking of \mathcal{PT} as a function of the parameters of the model. This can then be viewed as tuning an open system to achieve a stationary state where influx and outflux are balanced.

These features are nicely illustrated by the following \mathcal{PT} -symmetric two-level Hamiltonian [4]

$$H = \begin{pmatrix} -i\Gamma & g \\ g & i\Gamma \end{pmatrix}, \quad (1.1)$$

as we review in [8]. This system features both a \mathcal{PT} -symmetric and a \mathcal{PT} -broken regime. \mathcal{PT} -symmetry is intact when the hopping between the two levels, set by g , is faster than the inflow (outflow) of matter from (to) the exterior, fixed by Γ ; while it is broken in the regime where the inflow (outflow) is faster than the hopping and hence no stationary state is reached. As shown in Fig. 1, the energy levels of the system are real in the \mathcal{PT} -symmetric regime and complex in the \mathcal{PT} -broken phase. They meet at the so-called exceptional point $|\Gamma/g| = 1$.

Non-Hermitian Quantum Mechanics has seen a wide range of applications to

areas such as optics, cold atoms or condensed matters systems (see [9] for a review). Remarkably, applications to inhomogeneous condensed matter systems have been considered in [10].

In the context of Quantum Field Theory, non-Hermitian models have garnered great attention in recent years starting with the work [11]. The effect of non-Hermitian couplings has been extensively studied (see references in [12] for an overview), concluding that they can support real energy spectra, while also presenting novel phenomenology absent in Hermitian theories. Spacetime-dependent non-Hermitian couplings were first introduced in [1] where the spectrum was found to become complex at high energies while remaining real in the IR, thus signaling spontaneous breaking of \mathcal{PT} in the UV. This phenomenon was further explored in [12] where the authors discussed the stability of the solutions. Focusing now on strongly coupled holographic field theories [13–17], non-Hermitian systems were introduced in [18] and have been further explored in [19], where the authors constructed the phase diagram and computed the electrical conductivity; and in [20], where the effect of non-Hermitian quenches was studied. A review of these developments can be found in [8]. Non-Hermitian generalizations of the Sachdev-Ye-Kitaev model have also been studied in [21, 22].

In this paper we explore the effect of inhomogeneous non-Hermiticity. In particular, we follow the approach pioneered in [18] and consider a theory where the non-Hermiticity is introduced via the sources of an operator charged under a $U(1)$ symmetry and its Hermitian conjugate. The inhomogeneity is then achieved by taking the sources to be functions of one of the spatial coordinates, say, x^1 . Qualitatively, this setup describes a system where there is an x^1 -dependent influx and outflux of matter. Explicitly we construct a lattice where in all sites there is some x^1 -dependent inflow/outflow of matter, which we label *non-Hermitian lattice*. We also consider a Hermitian/non-Hermitian/Hermitian junction which we dub *non-Hermitian junction*. We explore the stability of the non-Hermitian lattice through quasinormal mode (QNM) analysis and discuss the null-energy condition (NEC). We find stable solutions that violate the NEC, in contrast with the observations of [19] for the homogeneous setup. Remarkably, for these solutions, close to the AdS-boundary the a -function [23–25] grows towards the bulk, suggesting an increase in the number of degrees of freedom along the renormalization group flow.

Strikingly, we find that our setups present a purely imaginary current that spontaneously breaks \mathcal{PT} . The existence of this current, absent in the homogeneous setup, indicates that the theory cannot be mapped to a Hermitian one through a Dyson map.

Despite the existence of a non-vanishing \mathcal{PT} -breaking current, in the low-temperature limit we recover a \mathcal{PT} -symmetric theory in the IR. Our model flows from a \mathcal{PT} -breaking UV to a \mathcal{PT} -symmetric IR. Hence an observer at low energies would see unitary evolution and only when exploring high energies would the non-unitarity be

manifest. This behaviour seems to be related to the irrelevant character of the spatial deformation as in e.g. [26–28]. Remarkably, despite the differences in the setup, our observation of \mathcal{PT} -symmetry restoration in the IR seems to agree with the results found in [1, 12].

The paper is structured as follows. In section 2 we present the holographic model. We pay special attention to the proper definition of \mathcal{PT} and to the construction of the Dyson map in both the CFT and the gravitational dual. In section 3 we define the non-Hermitian lattice, discuss the numerical setup and present our results. We distinguish two types of solutions: \mathcal{PT} -broken and \mathcal{PT} -unbroken. We also explicitly check that the latter can be described in terms of a Hermitian theory. In subsection 3.3 we compute the quasinormal frequencies for the \mathcal{PT} -broken solutions and discuss their stability. The NEC and the a -function are studied in subsection 3.4. To elucidate the ground state of the model, the low-temperature behaviour is studied in subsection 3.5. In section 4 we define the non-Hermitian junction and present some solutions. We find that the complex current found in the non-Hermitian lattice localizes at the junction. In section 5 we summarize our findings, present our conclusions and give an outlook on further studies. The holographic dictionary is constructed in appendix A and a detailed discussion of the calculation of the quasinormal frequencies can be found in appendix B.

2 Holographic Model

In this section we discuss the relevant aspects of our model. We begin by describing our setup from the CFT side, with special emphasis on the proper definition of \mathcal{PT} . We follow closely the discussion of [19]. Subsequently, we examine the action of the Dyson map from the CFT perspective and its relation to external gauge transformations. Next, we discuss the gravitational dual, presenting the relevant action, the equations of motion, the boundary conditions, and the holographic dictionary. The derivation of the latter can be found in appendix A. Lastly, we end this section by discussing the symmetries on the gravitational side of the duality and comparing them to those found in the CFT.

2.1 Non-Hermitian CFT

As stated in the introduction, we want to add non-Hermiticity through the sources \bar{s} and s of a scalar operator \mathcal{O} charged under a $U(1)$ symmetry and its Hermitian conjugate $\bar{\mathcal{O}}$. Thus, the relevant action to study should be

$$\mathcal{S} = \mathcal{S}_{\text{CFT}} + \int d^d x (\bar{s}\mathcal{O} + s\bar{\mathcal{O}}) = \int d^d x \mathcal{L}(x), \quad (2.1)$$

where \mathcal{S}_{CFT} is the action in absence of non-Hermitian sources and \mathcal{L} is the Lagrangian of the full theory.

Let us see that the action (2.1) is \mathcal{PT} -symmetric. We define the effect of \mathcal{PT} on the coordinates to be

$$x = (t, x^1, x^2, \dots, x^{d-1}) \xrightarrow{\mathcal{PT}} \mathcal{PT}x = (-t, -x^1, x^2, \dots, x^{d-1}), \quad (2.2)$$

where we take x^1 as the direction along which the inhomogeneities are present.¹

We choose \mathcal{O} to be a scalar under \mathcal{PT} , i.e.

$$\mathcal{O}(x) \xrightarrow{\mathcal{PT}} \mathcal{O}(\mathcal{PT}x), \quad \bar{\mathcal{O}}(x) \xrightarrow{\mathcal{PT}} \bar{\mathcal{O}}(\mathcal{PT}x), \quad (2.3)$$

meanwhile, the sources transform as conventional functions

$$s(x) \xrightarrow{\mathcal{PT}} s^*(\mathcal{PT}x), \quad \bar{s}(x) \xrightarrow{\mathcal{PT}} \bar{s}^*(\mathcal{PT}x). \quad (2.4)$$

Then, assuming that \mathcal{PT} acts trivially on \mathcal{S}_{CFT} and that s and \bar{s} are real, we conclude that the Lagrangian in the action (2.1) is a scalar under \mathcal{PT}

$$\mathcal{L}(x) \xrightarrow{\mathcal{PT}} \mathcal{L}(\mathcal{PT}x), \quad (2.5)$$

and thus that \mathcal{PT} is a symmetry of the quantum theory.² Remarkably the assumption of reality of the sources differs from demanding the theory to be Hermitian, as we can have real sources that do not satisfy $s^* = \bar{s}$. Hence, this setup does indeed allow for a straightforward implementation of non-Hermiticity.

Let us now take a moment to make explicit what would constitute spontaneous symmetry breaking (SSB) of \mathcal{PT} in this setup. We distinguish two possibilities for the vacuum to break \mathcal{PT}

- Sources are not invariant under \mathcal{PT} : In this case, $s^*(\mathcal{PT}x) \neq s(x)$ and/or $\bar{s}^*(\mathcal{PT}x) \neq \bar{s}(x)$. Therefore, although the Lagrangian is \mathcal{PT} -symmetric, we generically expect the vacuum to break \mathcal{PT} as we are imposing it explicitly through the sources.
- Sources are invariant under \mathcal{PT} . Here $s^*(\mathcal{PT}x) = s(x)$ and $\bar{s}^*(\mathcal{PT}x) = \bar{s}(x)$. Thus, we do not expect the vacuum to always break \mathcal{PT} as no external source breaks it. Hence, the SSB would be related to a dynamical process.

Clearly the former situation is not particularly interesting while the second possibility is much more physically relevant. For that reason, we will refer as SSB only to the second scenario.

¹Note that our definition of \mathcal{PT} differs from the conventional one employed in field theory in 4 spacetime dimensions. Our choice is motivated by the fact that for even number of spatial dimensions, the conventional definition is not valid as it yields a parity operation connected to the identity of the Lorentz group.

²Here we implicitly assume that the path integral measure is also invariant.

For later convenience, we also consider the possibility of adding to the action (2.1) a term coupling the $U(1)$ current to an external gauge field a_μ

$$\mathcal{S}' = \mathcal{S}_{\text{CFT}} + \int d^d x \left(\bar{s}\mathcal{O} + s\bar{\mathcal{O}} + a_\mu J^\mu \right). \quad (2.6)$$

The current and the gauge field transform under \mathcal{PT} as³

$$a_\mu(x) \xrightarrow{\mathcal{PT}} (-1)^\mu a_\mu^*(\mathcal{PT}x), \quad J^\mu(x) \xrightarrow{\mathcal{PT}} -(-1)^\mu J^\mu(\mathcal{PT}x), \quad (2.7)$$

where $(-1)^\mu = -1$ for $\mu = 0, 1$ and $+1$ otherwise. Hence the theory (2.6) is invariant under \mathcal{PT} provided that the external gauge field satisfies

$$-a_\mu^*(\mathcal{PT}x) = a_\mu(\mathcal{PT}x). \quad (2.8)$$

We stress that although the equation above indicates that \mathcal{PT} is broken for real external gauge fields, this is not in conflict with the use of real gauge fields in \mathcal{PT} -symmetric QFTs. The key point here is that a_μ is not a quantum field that fluctuates in the path integral, instead it is a classical 1-form that transforms under \mathcal{PT} as such.⁴ Hence the restrictions to a_μ are completely different from those imposed on a conventional $U(1)$ quantum gauge field.

2.2 Dyson map as an external gauge transformation

As stated in the introduction, in the \mathcal{PT} -symmetric phase, a non-Hermitian theory can be mapped to a Hermitian one through a Dyson map. This immediately ensures the existence of unitary evolution for some cleverly chosen inner product.

In general constructing the Dyson map in a field theory is a highly non-trivial task. However, as shown in [20], for our model we can easily determine the inverse Dyson map starting from the Hermitian case.

Let us consider a Hermitian theory with action (2.1) and $s = \bar{s} = M$. To obtain a non-Hermitian theory we could consider the similarity transformation such that

$$\mathcal{O} \rightarrow S\mathcal{O}, \quad \bar{\mathcal{O}} \rightarrow S^{-1}\bar{\mathcal{O}}, \quad (2.9)$$

where $S = e^{\beta(x)}$ is a complexified $U(1)$ transformation. At leading order, this transformation yields the following non-Hermitian action

$$\mathcal{S} = \mathcal{S}_{\text{CFT}} + \int d^d x \left(MS\mathcal{O} + MS^{-1}\bar{\mathcal{O}} + \frac{i}{q}(S^{-1}\partial_\mu S)J^\mu + O(S^{-1}\partial_\mu S)^2 \right), \quad (2.10)$$

³Note that these are the usual transformation rules for a current operator and an external 1-form gauge field. The only remarkable feature is that we allow for the external gauge field to be a complex function. As we will see, this complexification plays an important role in the construction of the Dyson map.

⁴Under \mathcal{PT} an external 1-form $a = a_\mu dx^\mu$ transforms as a function, i.e.,

$$a(x) \xrightarrow{\mathcal{PT}} a^*(\mathcal{PT}x) = a_\mu^*(\mathcal{PT}x)d(\mathcal{PT}x)^\mu$$

Hence the component a_μ satisfies $a_\mu(x) \xrightarrow{\mathcal{PT}} (-1)^\mu a_\mu^*(\mathcal{PT}x)$.

where q is the $U(1)$ charge of \mathcal{O} and J^μ is the $U(1)$ current. This action has the form of (2.6) as $iq^{-1}S^{-1}\partial_\mu S$ behaves as an external gauge field. The term proportional to the current follows from the existence of the $U(1)$ symmetry in \mathcal{S}_{CFT} . We know that if S were to be a conventional infinitesimal $U(1)$ matrix, the variation of \mathcal{S}_{CFT} under (2.9) would give a term $iq^{-1}(S^{-1}\partial_\mu S)J^\mu$ plus higher order corrections; all of which could be eliminated by coupling the theory to a $U(1)$ gauge field. However, now under the complexified $U(1)$, the gauge field needed to eliminate the extra terms cannot consistently be made into a dynamical quantum gauge field, instead it will be an external classical gauge field [12].

In terms of the external sources s, \bar{s} and the external gauge field a_μ we can construct a Dyson map as the following external gauge transformation

$$s \rightarrow sS^{-1}, \quad \bar{s} \rightarrow \bar{s}S, \quad a_\mu \rightarrow a_\mu + \frac{i}{q}S^{-1}\partial_\mu S, \quad (2.11)$$

with S chosen to bring the action to the form (2.1) with $s = \bar{s}$.

2.3 Gravitational dual

For our holographic model, we consider the 4-dimensional minimal model introduced in [18], whose bulk action is given by

$$\mathcal{S} = \int d^4y \sqrt{-g} \left(R - 2\Lambda - \frac{1}{4}F_{MN}F^{MN} - \mathcal{D}_M\phi\mathcal{D}^M\bar{\phi} - m^2\phi\bar{\phi} - \frac{v}{2}\phi^2\bar{\phi}^2 \right), \quad (2.12)$$

where ϕ and $\bar{\phi}$ are scalars charged under a $U(1)$ symmetry, A is the gauge field of the $U(1)$ symmetry, $F = dA$ is the field strength tensor, $\Lambda = -3/l^2$ is the cosmological constant and l is the AdS radius, which we set to unity. The scalar mass is taken to be $m^2 = -2$ and the coupling $v = 3$. The action of the $U(1)$ transformation is

$$\phi \rightarrow e^{-iq\alpha}\phi, \quad \bar{\phi} \rightarrow e^{iq\alpha}\bar{\phi}, \quad A_M \rightarrow A_M - \partial_M\alpha, \quad (2.13)$$

and the covariant derivatives are defined as

$$\mathcal{D}_M\phi = \partial_M\phi - iqA_M\phi, \quad \mathcal{D}_M\bar{\phi} = \partial_M\bar{\phi} + iqA_M\bar{\phi}, \quad (2.14)$$

where q is the scalar charge.

The equations of motion derived from the action (2.12) are

$$\mathcal{M}_N = \nabla_M F^M_N + iq(\phi\mathcal{D}_N\bar{\phi} - \bar{\phi}\mathcal{D}_N\phi) = 0, \quad (2.15a)$$

$$\mathcal{F} = (\nabla_M - iqA_M)\mathcal{D}^M\phi - m^2\phi - v\phi^2\bar{\phi} = 0, \quad (2.15b)$$

$$\bar{\mathcal{F}} = (\nabla_M + iqA_M)\mathcal{D}^M\bar{\phi} - m^2\bar{\phi} - v\bar{\phi}^2\phi = 0, \quad (2.15c)$$

$$\mathcal{E}_{MN} = R_{MN} - \Lambda g_{MN} - \frac{1}{2}\left(T_{MN} - \frac{1}{2}g_{MN}T^P_P\right) = 0, \quad (2.15d)$$

where the bulk energy-momentum tensor is given by

$$T_{MN} = F_{PM} F^P{}_N + 2\mathcal{D}_{(M}\phi\mathcal{D}_{N)}\bar{\phi} - g_{MN} \left(\frac{1}{4}F_{PQ}F^{PQ} + \mathcal{D}_P\phi\mathcal{D}^P\bar{\phi} + m^2\phi\bar{\phi} + \frac{v}{2}\phi^2\bar{\phi}^2 \right). \quad (2.16)$$

We are interested in static solutions at nonzero temperature and vanishing chemical potential with inhomogeneities along the direction x^1 only. Hence, we choose the following ansatz compatible with those assumptions [29]

$$\begin{aligned} ds^2 &= \frac{1}{z^2} \left[- (1 - z^3) h_1 dt^2 + h_3 (dx^1 + h_5 dz)^2 + h_4 (dx^2)^2 + \frac{h_2}{1 - z^3} dz^2 \right], \\ h_1 &= h_1(x^1, z), \quad h_2 = h_2(x^1, z), \quad h_3 = h_3(x^1, z), \\ h_4 &= h_4(x^1, z), \quad h_5 = h_5(x^1, z), \\ \phi &= \phi(x^1, z), \quad \bar{\phi} = \bar{\phi}(x^1, z), \quad A = A_1(x^1, z) dx^1. \end{aligned} \quad (2.17)$$

where z is the holographic radial coordinate. The AdS boundary is located at $z = 0$ and we have a black brane horizon at $z = 1$.

Regarding the boundary conditions, at the AdS boundary we impose

$$\begin{aligned} ds^2(z \rightarrow 0) &= \frac{1}{z^2} [-dt^2 + (dx^1)^2 + (dx^2)^2 + dz^2], \\ \partial_z \phi(x^1, 0) &= s(x^1), \quad \partial_z \bar{\phi}(x^1, 0) = \bar{s}(x^1), \quad A_1(x^1, 0) = a_1(x^1), \end{aligned} \quad (2.18)$$

where s , \bar{s} and a_1 are the external sources and gauge field in the action (2.6).

Throughout this paper we focus only on two distinct cases characterized by the values of s , \bar{s} and a_1

A. Here we take the following parameters

$$s = (1 - \eta)M, \quad \bar{s} = (1 + \eta)M, \quad a_1 = 0, \quad (2.19)$$

where M is a constant and $\eta = \eta(x^1)$ is a function representing the non-Hermiticity.

B. In this case we instead take the family of sources

$$s = (1 - \eta)M, \quad \bar{s} = (1 + \eta)M, \quad a_1 = \frac{i}{q} \frac{\eta'}{1 - \eta^2}, \quad (2.20)$$

which, following the discussion of section 2.2 can be mapped through a Dyson map to the Hermitian case

$$s = \sqrt{1 - \eta^2}M, \quad \bar{s} = \sqrt{1 - \eta^2}M, \quad a_1 = 0. \quad (2.21)$$

Note that case B is ill-defined if $|\eta(x^1)| = 1$ as a_1 in (2.20) diverges. Moreover, the alternative picture (2.21) obtained through the Dyson map, also ceases to be \mathcal{PT} -symmetric and Hermitian as the sources s and \bar{s} become complex. Hence, as we would like the non-Hermiticity parametrized by η to be a feature that we can continuously turn on starting from the Hermitian case with $\eta = 0$; we only consider $|\eta(x^1)| < 1$ in case B for consistency. On the other hand, in case A we can, a priori, take $|\eta(x^1)| \geq 1$ without any apparent issues. However, as we will see, the regime $|\eta(x^1)| \geq 1$ does not admit solutions with real metrics for all values of η .

To conclude this section we summarize here the relevant holographic dictionary needed to analyze the dual CFT. An explicit derivation can be found in appendix A. Using the following asymptotic expansion for the fields

$$h_1(x^1, z) = 1 - \frac{1}{4}s(x^1)\bar{s}(x^1)z^2 + h_1^{(3)}(x^1)z^3 + \dots, \quad (2.22a)$$

$$h_2(x^1, z) = 1 - \frac{1}{3}\left[h_1^{(3)}(x^1) + h_3^{(3)}(x^1) + h_4^{(3)}(x^1)\right]z^3 + \dots, \quad (2.22b)$$

$$h_3(x^1, z) = 1 - \frac{1}{4}s(x^1)\bar{s}(x^1)z^2 + h_3^{(3)}(x^1)z^3 + \dots, \quad (2.22c)$$

$$h_4(x^1, z) = 1 - \frac{1}{4}s(x^1)\bar{s}(x^1)z^2 + h_4^{(3)}(x^1)z^3 + \dots, \quad (2.22d)$$

$$h_5(x^1, z) = \frac{1}{8}\partial_1[\bar{s}(x^1)s(x^1)]z^3 + \dots, \quad (2.22e)$$

$$\phi(x^1, z) = s(x^1)z + \phi^{(2)}(x^1)z^2 + \dots, \quad (2.22f)$$

$$\bar{\phi}(x^1, z) = \bar{s}(x^1)z + \bar{\phi}^{(2)}(x^1)z^2 + \dots, \quad (2.22g)$$

$$A_1(x^1, z) = a_1(x^1) + A_1^{(1)}(x^1)z + \dots, \quad (2.22h)$$

obtained from solving the equations of motion for $z \rightarrow 0$; we conclude that the vacuum expectation values (VEVs) of the operators \mathcal{O} and $\bar{\mathcal{O}}$, the current J_1 , and the boundary energy-momentum tensor $T_{\mu\nu}$; are given by

$$\begin{aligned} \langle J_1 \rangle &= A_1^{(1)}, & \langle \mathcal{O} \rangle &= \phi^{(2)}, & \langle \bar{\mathcal{O}} \rangle &= \bar{\phi}^{(2)}, \\ \langle T_{tt} \rangle &= 2 - \frac{2}{3}h_1^{(3)} + \frac{7}{3}(h_3^{(3)} + h_4^{(3)}) + s\bar{\phi}^{(2)} + \bar{s}\phi^{(2)}, \\ \langle T_{11} \rangle &= 1 + \frac{2}{3}h_3^{(3)} - \frac{7}{3}(h_1^{(3)} + h_4^{(3)}) - s\bar{\phi}^{(2)} - \bar{s}\phi^{(2)}, \\ \langle T_{22} \rangle &= 1 + \frac{2}{3}h_4^{(3)} - \frac{7}{3}(h_1^{(3)} + h_3^{(3)}) - s\bar{\phi}^{(2)} - \bar{s}\phi^{(2)}. \end{aligned} \quad (2.23)$$

Moreover, we also find the following Ward identity associated with the $U(1)$ symmetry of the boundary CFT

$$\partial_1 \langle J_1 \rangle = iq \left(s \langle \bar{\mathcal{O}} \rangle - \bar{s} \langle \mathcal{O} \rangle \right). \quad (2.24)$$

2.4 Matching symmetries

Lastly, to conclude our description of the holographic model, we describe the matching of symmetries between the CFT and gravitational dual in greater detail.

First, let us note that a z -independent gauge transformation (2.13) leaves the action (2.12) invariant but changes the boundary conditions as in (2.11). Hence, we conclude that, as expected from the usual holographic prescription, the external gauge transformations in the Dyson map correspond to complexified local gauge transformations in the gravitational dual.

Regarding \mathcal{PT} , in the gravitational dual we have the following transformation rules inherited from the corresponding dual operators

$$y = (x, z) = (t, x^1, x^2, z) \xrightarrow{\mathcal{PT}} \mathcal{PT}y = (\mathcal{PT}x, z) = (-t, -x^1, x^2, z), \quad (2.25a)$$

$$\phi(y) \xrightarrow{\mathcal{PT}} \phi(\mathcal{PT}y), \quad \bar{\phi}(y) \xrightarrow{\mathcal{PT}} \bar{\phi}(\mathcal{PT}y), \quad A_1(y) \xrightarrow{\mathcal{PT}} A_1(\mathcal{PT}y). \quad (2.25b)$$

Thus, the action (2.12) is trivially invariant under \mathcal{PT} . However, we also need to account for the boundary conditions (2.18) which might break \mathcal{PT} . Under \mathcal{PT} they transform as

$$\partial_z \phi(x, 0) = s(x) \xrightarrow{\mathcal{PT}} \partial_z \phi(\mathcal{PT}x, 0) = s^*(\mathcal{PT}x), \quad (2.26a)$$

$$\partial_z \bar{\phi}(x, 0) = \bar{s}(x) \xrightarrow{\mathcal{PT}} \partial_z \bar{\phi}(\mathcal{PT}x, 0) = \bar{s}^*(\mathcal{PT}x), \quad (2.26b)$$

$$A_1(x, 0) = a_1(x) \xrightarrow{\mathcal{PT}} A_1(\mathcal{PT}x, 0) = -a_1^*(\mathcal{PT}x), \quad (2.26c)$$

where \bar{s} , s have been treated as functions under \mathcal{PT} and a_1 as an external gauge field. Then, in order for the theory to be invariant under \mathcal{PT} as in (2.5), we conclude that we have to restrict ourselves to

$$s(x) = s^*(x), \quad \bar{s}(x) = \bar{s}^*(x), \quad -a_1^*(x) = a_1(x), \quad (2.27)$$

which remarkably matches the criteria derived in section 2.1. In the following, to ensure that the sources do not explicitly break \mathcal{PT} we further restrict s , \bar{s} to be even functions of x^1 .

3 Non-Hermitian lattice

In this section we consider η to be a smooth, even, periodic function with period L . Physically, we consider that this setup describes a lattice with lattice constant L , where there is inflow/outflow that smoothly extends throughout each site. For simplicity we take η to be a cosine function

$$\eta(x^1) = a \cos\left(\frac{2\pi}{L}x^1\right), \quad (3.1)$$

and we study solutions for different values of a .

It is worth noting that, due to the conformal symmetry of the UV, our results depend only on dimensionless quantities. Thus, without loss of generality, we choose to parametrize them in terms of $\{a, T/M, LM, q\}$. Moving forward, we set $LM = 3$ and $q = 1$ unless stated otherwise. This allows us to characterize the solutions by their temperature T/M and the amplitude a .

3.1 Numerical method

In order to solve the equations of motion (2.15), we employ the DeTurck trick to make the Einstein equations (2.15d) elliptic [30–32]. In summary, this trick consists of replacing the Einstein equations by the Einstein-DeTurck equations

$$R_{MN} - \Lambda g_{MN} - \frac{1}{2} \left(T_{MN} - \frac{1}{2} T^P{}_P g_{MN} \right) - \nabla_{(M} \xi_{N)} = 0, \quad (3.2)$$

where $\xi^P = g^{MN} (\Gamma^P{}_{MN} - \bar{\Gamma}^P{}_{MN})$ with Γ and $\bar{\Gamma}$ the Christoffel symbols of the metric we are solving for (target metric) and of a reference metric, respectively. The Einstein-DeTurck equations are hyperbolic by construction and thus they are numerically better behaved. Hence we choose to solve them and check that the DeTurck term vanishes for the solution; thus ensuring that it is also a solution to the Einstein equations. Numerically we guarantee this by checking that the DeTurck constraint $\xi_M \xi^M$ is smaller than a given tolerance. We refer the reader to [32] for further details on this method.

Importantly, the reference metric should have the same asymptotic behaviour as the target metric. Thus we choose the reference metric to be given by

$$ds^2 = \frac{1}{z^2} \left[- (1 - z^3) dt^2 + (dx^1)^2 + (dx^2)^2 + \frac{dz^2}{1 - z^3} \right]. \quad (3.3)$$

Besides employing DeTurck’s trick, we also note that when solving Maxwell’s equations (2.15a) we get a constraint and two second-order equations. We choose to only solve the second-order equations and check that the constraint is satisfied for the solutions up to a given tolerance.

With all this in mind, we discretize the system using a Chebyshev grid in the z direction and a Fourier grid with periodicity L on the x^1 direction. We solve the final equations using the Newton-Raphson method. All numerical calculations have been carried out using *Mathematica*.

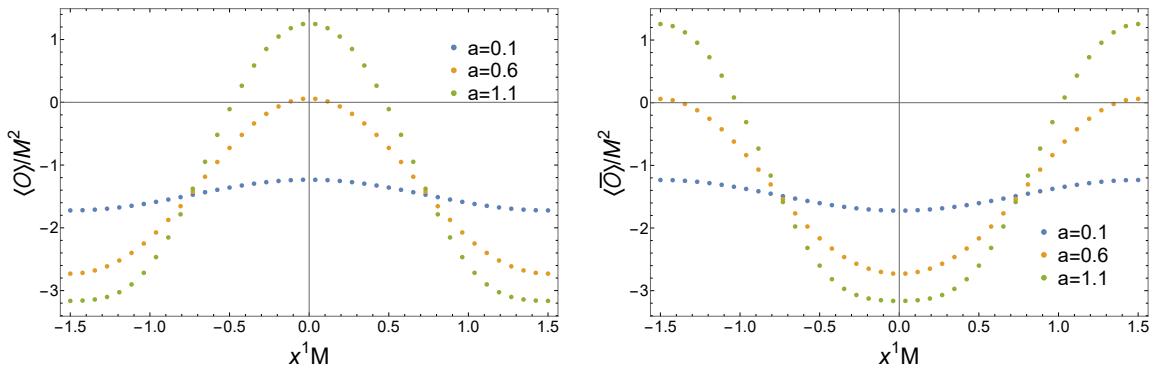
3.2 Numerical solutions

As indicated in section 2.3, we distinguish between two scenarios A and B, defined by equations (2.19) and (2.20), respectively. We label scenario A as the \mathcal{PT} -broken phase and B as the \mathcal{PT} -unbroken phase, for reasons that will become apparent below.

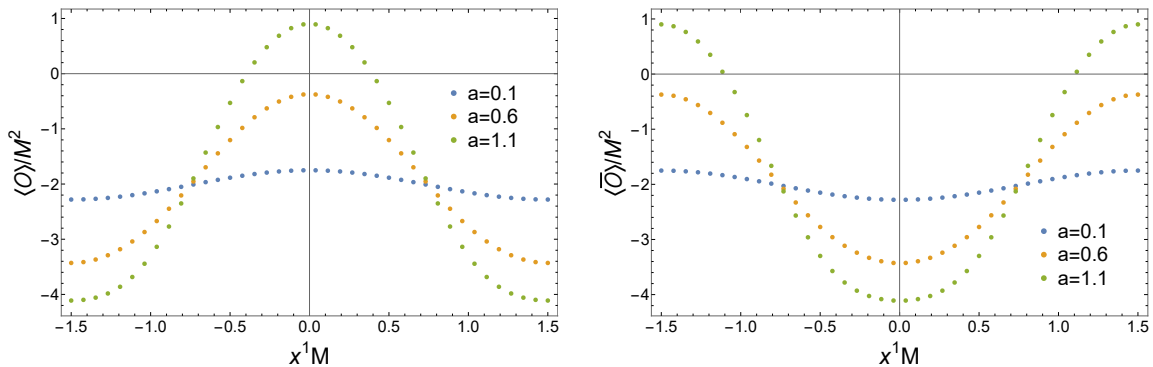
Regarding the numerics, in this section we employ a Chebyshev grid with 20 points for the z direction and a Fourier grid with 40 points for the x^1 direction; we demand a tolerance of 10^{-8} in both the Newton-Raphson method as well as for the DeTurck constraint and the constraint arising from the Maxwell equations.

3.2.1 \mathcal{PT} broken phase

In figures 2-4 we plot the expectation values of the condensates $\langle \mathcal{O} \rangle$, $\langle \bar{\mathcal{O}} \rangle$, the current $\langle J_1 \rangle$ and the energy density $\langle T_{tt} \rangle$ for amplitudes $a = \{0.1, 0.6, 1.1\}$ and temperatures



(a) $T/M = 0.5$



(b) $T/M = 1$

Figure 2: Expectation values of the condensates $\langle \mathcal{O} \rangle$ and $\langle \bar{\mathcal{O}} \rangle$ in the \mathcal{PT} -broken phase.

$T/M = \{0.5, 1\}$. We observe that the inhomogeneous non-Hermiticity yields a purely imaginary current which was previously absent in the homogeneous setup. Most notably this current is an odd function of x^1 and thus spontaneously breaks \mathcal{PT}

$$\langle J_1(x) \rangle \xrightarrow{\mathcal{PT}} \langle J_1(\mathcal{PT}x) \rangle = -\langle J_1(x) \rangle \neq \langle J_1(x) \rangle, \quad (3.4)$$

indicating that this model cannot be mapped via the Dyson map (2.11) to a purely Hermitian theory. We can better understand this by noting the following: we can use the Dyson map (2.11) with $S = \sqrt{\frac{1-\eta}{1+\eta}}$ to have $s = \bar{s} = \sqrt{1-\eta^2}M$ and thus eliminate the non-Hermiticity from the sources. However, by doing so we introduce a purely imaginary external gauge field a_1 , proportional to $\partial_1\eta$, which couples to the current J_1 , which is a Hermitian operator. Hence, even if we remove the non-Hermiticity from the sources of \mathcal{O} and $\bar{\mathcal{O}}$, the Lagrangian always remains non-Hermitian as long as $\partial_1\eta \neq 0$.

Interestingly, we cannot find solutions with real metric for all values of η . Indeed, as illustrated in figure 5 where we plot the mean of $\langle \mathcal{O} \rangle$ as a function of a , we observe that there is a maximum a_{\max} beyond which solutions are not found. This behaviour

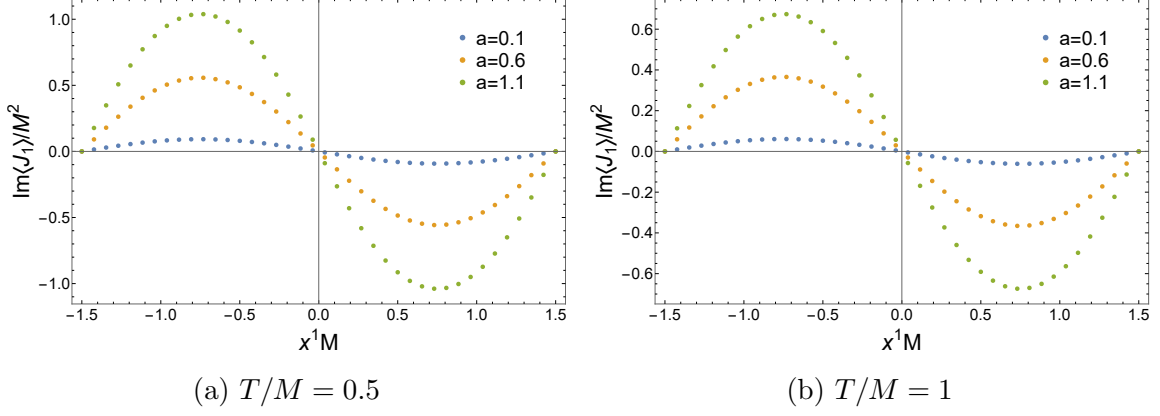


Figure 3: Imaginary part of the expectation value of the current $\langle J_1 \rangle$ in the \mathcal{PT} -broken phase. The real part is zero for any $\{a, T/M\}$.

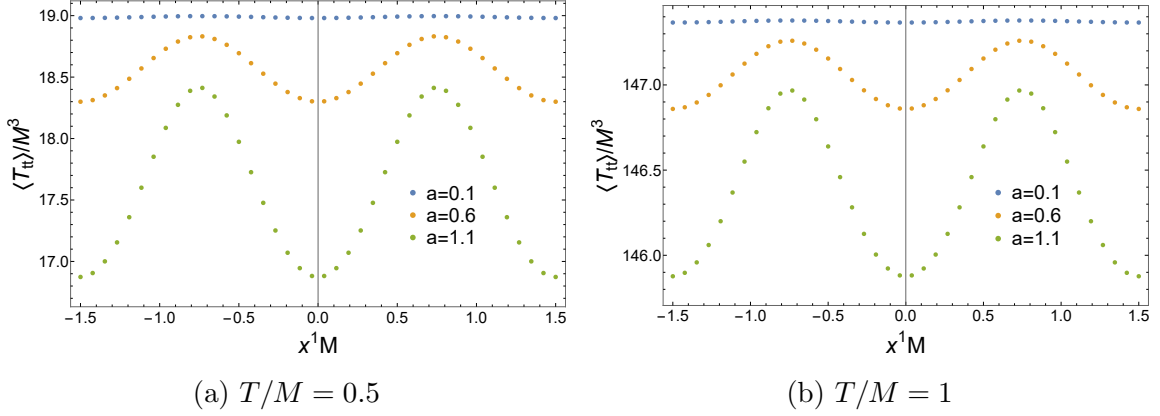


Figure 4: Expectation value of the energy density $\langle T_{tt} \rangle$ in the \mathcal{PT} -broken phase.

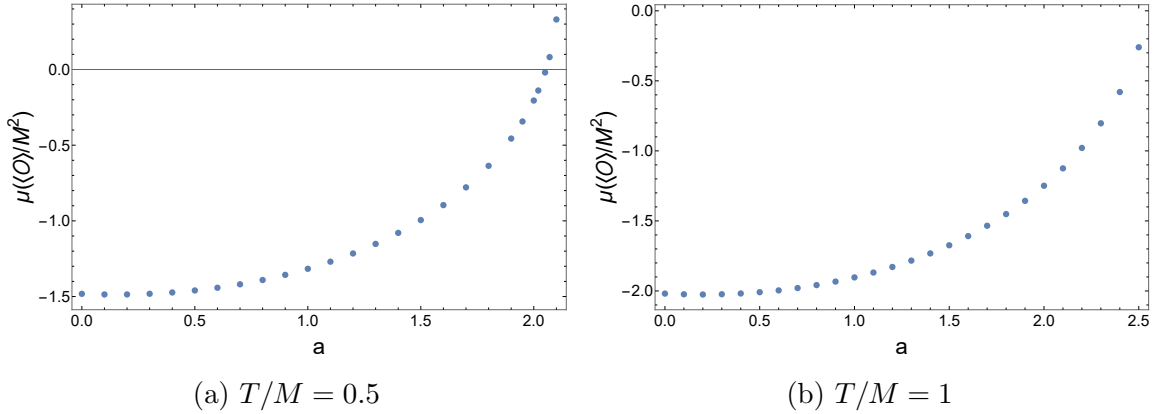


Figure 5: Mean of the condensate $\mu(\langle \mathcal{O} \rangle)$ in the \mathcal{PT} -broken phase as a function of the amplitude a . We do not find solutions with real metric for $a > a_{\max} \approx 2.1$ in (a) and $a > a_{\max} \approx 2.5$ in (b). We note that $\mu(\langle \mathcal{O} \rangle) = \mu(\langle \bar{\mathcal{O}} \rangle)$.

is very reminiscent of the one observed in the homogeneous setup in [18]. However, as we will see in the next section, we observe that in our setup, some of the solutions with $\max|\eta| > 1$ are linearly stable.

We note that as is standard in \mathcal{PT} -broken phases, there exist two phases related by complex conjugation. The complex conjugated phase to the one presented here arises by exchanging $s \leftrightarrow \bar{s}$ and has the \mathcal{PT} -conjugated current, namely see (3.4) $\langle J_1(x) \rangle \rightarrow -\langle J_1(x) \rangle$.

3.2.2 \mathcal{PT} unbroken phase

In figures 6-8 we plot the expectation values of the condensates $\langle \mathcal{O} \rangle$, $\langle \bar{\mathcal{O}} \rangle$, the current $\langle J_1 \rangle$ and the energy density $\langle T_{tt} \rangle$ for amplitudes $a = \{0.1, 0.6\}$ and temperatures $T/M = \{0.5, 1\}$.⁵ In this case, we observe that the current $\langle J_1 \rangle$ vanishes and hence that \mathcal{PT} is not broken. This guarantees the existence of a Dyson map to a purely Hermitian theory. Indeed, as indicated in section (2.3), we can perform a Dyson map (2.11) with $S = \sqrt{\frac{1-\eta}{1+\eta}}$ to obtain a Hermitian \mathcal{PT} -symmetric theory with sources (2.21). In order to explicitly check the equivalence between both descriptions, we would like to compare the VEVs $\langle \mathcal{O} \rangle_{\text{H}}$ and $\langle \bar{\mathcal{O}} \rangle_{\text{H}}$ computed in the Hermitian theory (2.21) to the VEVs $\langle \mathcal{O} \rangle_{\text{NH}}$ and $\langle \bar{\mathcal{O}} \rangle_{\text{NH}}$ computed in the non-Hermitian one (2.20). We can do so by recalling that the Dyson map (2.11), which we identified with an external gauge transformation, can also be regarded as a similarity transformation (2.9) generated by an operator \mathcal{Q} such that

$$\mathcal{Q}\mathcal{O}\mathcal{Q}^{-1} = S\mathcal{O}, \quad \mathcal{Q}\bar{\mathcal{O}}\mathcal{Q}^{-1} = S^{-1}\bar{\mathcal{O}}, \quad (3.5)$$

$$\mathcal{Q}\mathcal{S}[s, \bar{s}, a_\mu]\mathcal{Q}^{-1} = \mathcal{S}\left[S^{-1}s, S\bar{s}, a_\mu + \frac{i}{q}S^{-1}\partial_\mu S\right]. \quad (3.6)$$

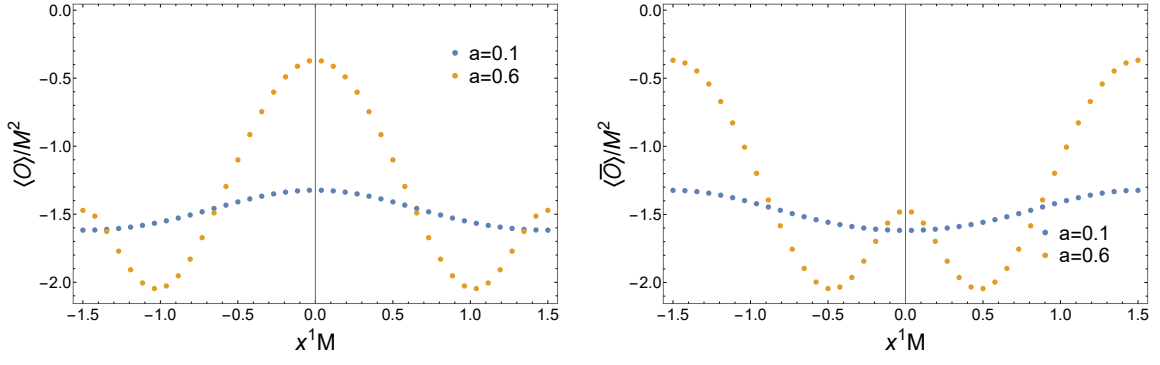
Then, as the trace is invariant under similarity transformations we have that

$$\begin{aligned} \langle \bar{\mathcal{O}} \rangle_{\text{NH}} &= \text{Tr}[\bar{\mathcal{O}}e^{-\beta H_{\text{NH}}}] = \text{Tr}[\mathcal{Q}\bar{\mathcal{O}}e^{-\beta H_{\text{NH}}}\mathcal{Q}^{-1}] = \text{Tr}[S^{-1}\bar{\mathcal{O}}e^{-\beta H_{\text{H}}}] = S^{-1}\langle \bar{\mathcal{O}} \rangle_{\text{H}}, \\ \langle \mathcal{O} \rangle_{\text{NH}} &= \text{Tr}[\mathcal{O}e^{-\beta H_{\text{NH}}}] = \text{Tr}[\mathcal{Q}\mathcal{O}e^{-\beta H_{\text{NH}}}\mathcal{Q}^{-1}] = \text{Tr}[S\mathcal{O}e^{-\beta H_{\text{H}}}] = S\langle \mathcal{O} \rangle_{\text{H}}. \end{aligned} \quad (3.7)$$

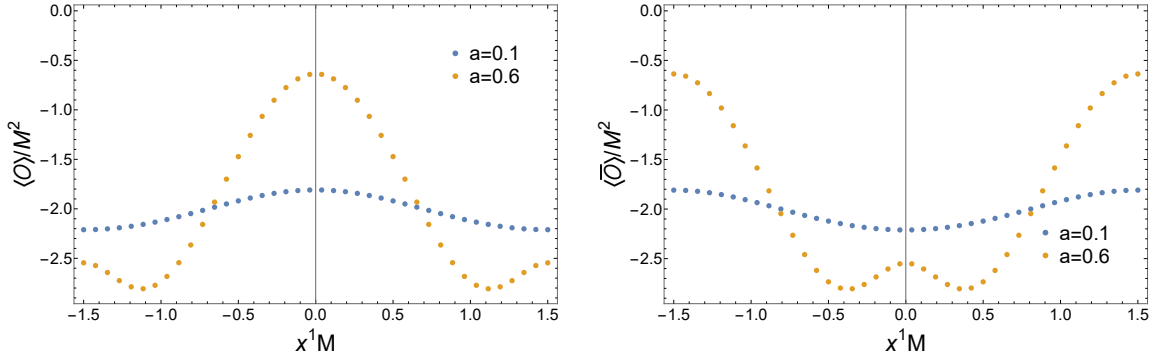
where H_{H} and H_{NH} are the generators of time evolution, i.e. the Hamiltonians, in the Hermitian and non-Hermitian theories, respectively.

Then, provided we can equivalently use the non-Hermitian and Hermitian descriptions, we should find that $\langle \mathcal{O} \rangle_{\text{NH}} = S\langle \mathcal{O} \rangle_{\text{H}}$ and $\langle \bar{\mathcal{O}} \rangle_{\text{NH}} = S^{-1}\langle \bar{\mathcal{O}} \rangle_{\text{H}}$ for $S = \sqrt{\frac{1-\eta}{1+\eta}}$. This is confirmed by figure 9 where we clearly see that for $\{a, T/M\} = \{0.6, 1\}$ the equivalence is indeed satisfied.

⁵Recall that in this setup, which corresponds to scenario B in section 2.3, we restrict $|\eta(x^1)| < 1$ as discussed in the aforementioned section. For η given by (3.1) this implies that we must take $|a| < 1$.

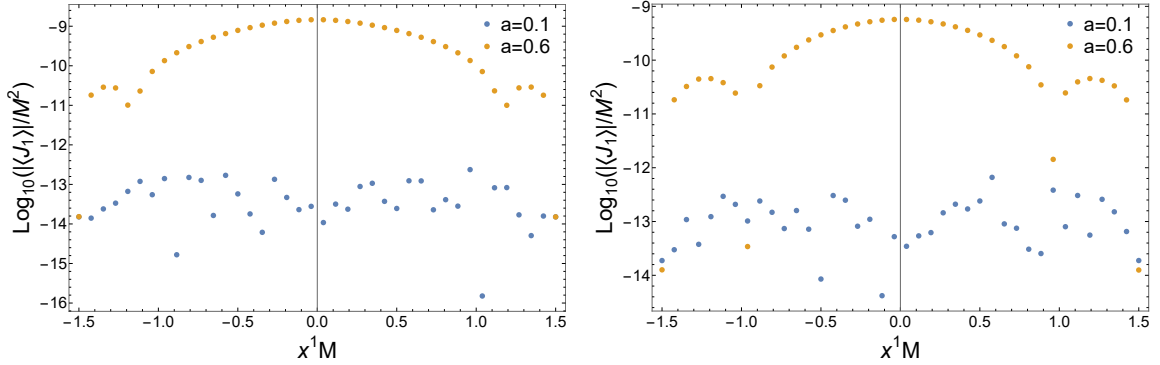


(a) $T/M = 0.5$



(b) $T/M = 1$

Figure 6: Expectation values of the condensates $\langle \mathcal{O} \rangle$ and $\langle \bar{\mathcal{O}} \rangle$ in the \mathcal{PT} -unbroken phase.



(a) $T/M = 0.5$

(b) $T/M = 1$

Figure 7: Absolute value of the expectation value of the current $\langle J_1 \rangle$ in the \mathcal{PT} -unbroken phase. Note that in both plots the current vanishes up to the accuracy of the numerics.

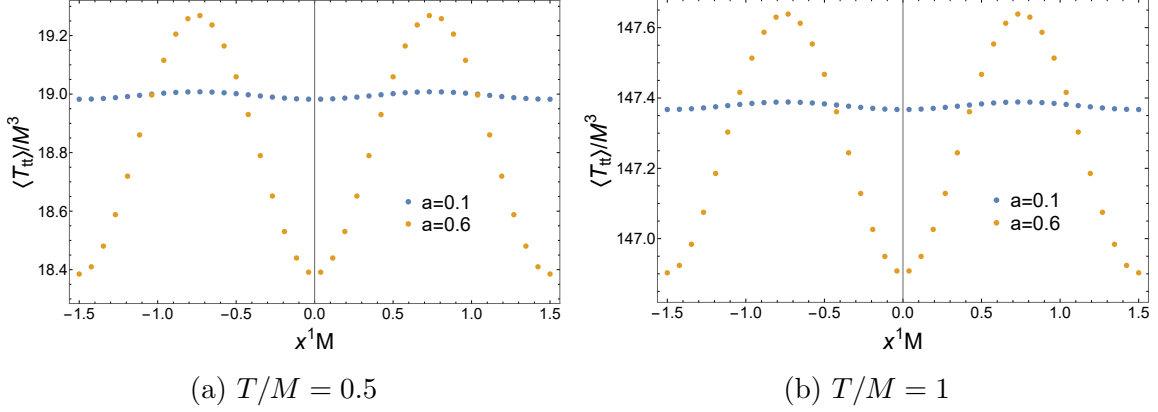


Figure 8: Expectation value of the energy density $\langle T_{tt} \rangle$ in the \mathcal{PT} -unbroken phase.

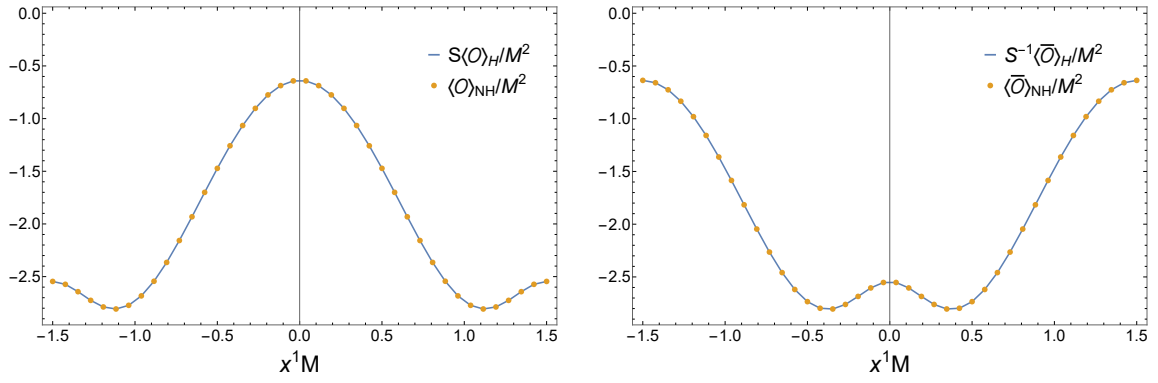


Figure 9: Comparison between the Hermitian and non-Hermitian descriptions for the \mathcal{PT} -unbroken phase at $\{a, T/M\} = \{0.6, 1\}$.

3.3 Quasinormal frequencies and stability

In order to assess the stability of the solutions we have found in the previous section, we study the quasinormal frequencies (QNFs) of the system, looking for potential instabilities. As the \mathcal{PT} -unbroken phase is equivalent to a Hermitian theory, which we do not expect to be unstable, here we focus only on the \mathcal{PT} -broken phase.

QNFs are the eigenfrequencies of the linearized fluctuations over our background solution which satisfy infalling boundary conditions at the horizon and sourceless boundary conditions at the AdS boundary. Consequently, we choose to write the corresponding quasinormal modes (QNMs) as

$$\delta\varphi = \delta\varphi(x^1, z)e^{-i\omega t + ikx^1}, \quad (3.8)$$

where φ denotes any field of the gravity side satisfying the aforementioned boundary conditions, ω is the QNF and k is the momentum.⁶ Due to the periodic structure of the lattice, the momentum k satisfies $k \sim k + \frac{2\pi}{L}$.

⁶Our definition of the QNMs is motivated by the usual Bloch decomposition frequently used in

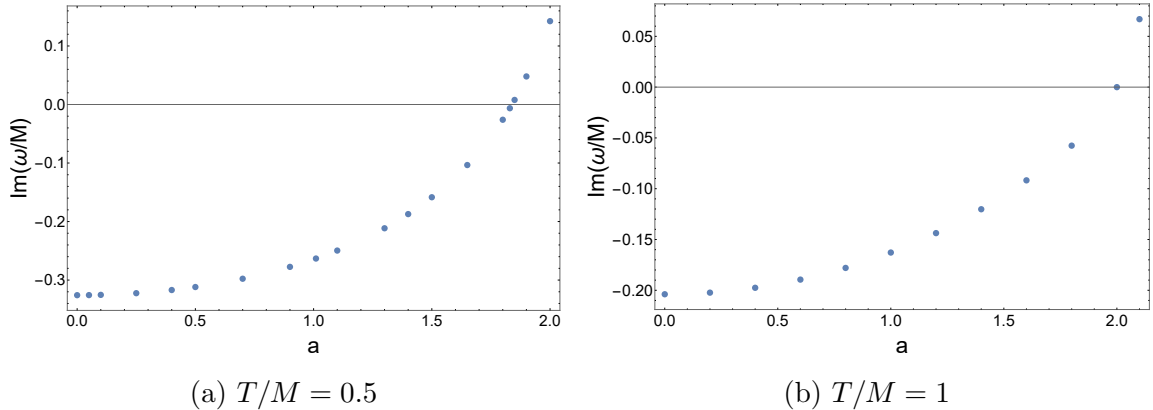


Figure 10: Imaginary part of the lowest lying QNF for the \mathcal{PT} -broken solutions at small but nonzero momentum k/M . Concretely, in (a) the momentum is $k/M = \frac{2\pi}{3} \cdot 10^{-4}$ and in (b) it is $k/M = \frac{4\pi}{3} \cdot 10^{-4}$. Stable solutions are found for $a \lesssim 1.8$ in (a) and $a \lesssim 2$ in (b).

As we defined QNMs without any momentum in the x^2 direction, we are not breaking the reflection symmetry along the x^2 direction. Hence, we can decouple fluctuations into two sectors characterized by their transformation rules under reflections along the x^2 axis

- i. Odd: Changes sign under reflection along x^2 .
- ii. Even: Does not change sign under reflection along x^2 .

A detailed discussion on the numerical method and the subtleties involved in the computation of the QNFs can be found in appendix B. Henceforth we focus only on the even sector as we have found it to be the only one playing a relevant role in the stability analysis.

In figure 10 we present the imaginary part of the lowest lying QNFs in the even sector as a function of a for $T/M = 0.5$ and $T/M = 1$. Remarkably, we find that the \mathcal{PT} -breaking solutions are always stable for $a < 1$. This indicates that the existence of a \mathcal{PT} -breaking current does not generically drive the system unstable. Eventually, for some $a > 1$ but smaller than the a_{max} defined in the previous section, instabilities kick in. Remarkably, this indicates that there are stable solutions that locally have $|\eta(x^1)| > 1$. This contrasts with the homogeneous case, where solutions were found to be unstable the moment $|\eta|$ crossed 1. It would be interesting to study how the existence and stability of solutions with $|\eta(x^1)| > 1$ depends on temperature T/M and system size LM . This would be numerically intensive and we leave it for future work.

solid state physics. As the lattice is periodic we can write any eigenfunction as a plane wave with momentum k in the first Brillouin zone times a periodic function.

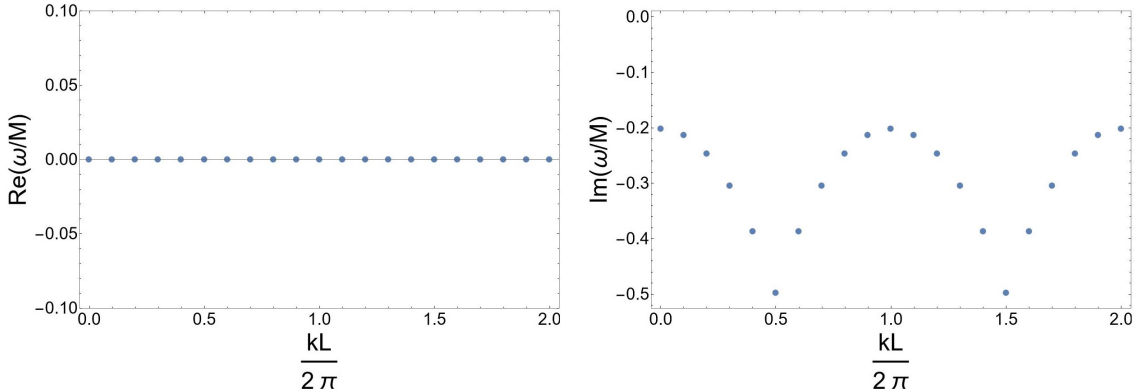


Figure 11: Dependence of the lowest lying QNF on the dimensionless momentum kL .

In figure 11 we plot real and imaginary parts of the lowest lying QNF at $\{a, T/M\} = \{0.2, 1\}$ as a function of the dimensionless momentum $kL = 3k/M$. We note that the equivalence relation $k \sim k + \frac{2\pi}{L}$, arising from the lattice structure, manifests itself in the periodicity of the QNF. This confirms that we only need to consider momenta in the first Brillouin zone to describe the system. Within this first Brillouin zone we observe that the real part of the QNF is always zero and that the imaginary part decreases to a minimum $\text{Im}(\omega/M) \approx -0.5$ and then rises back again to a maximum $\text{Im}(\omega/M) \approx -0.2$.

3.4 Null energy condition

We have found that in the \mathcal{PT} -broken regime we can have stable solutions with $|\eta| > 1$ in some region of space. Now, in this subsection we further explore the nature of such solutions by studying whether they violate the bulk null energy condition (NEC)

$$T_{MN} u^M u^N \geq 0, \quad (3.9)$$

where u is any vector tangent to a null geodesic.

Let us commence by performing a near-boundary analysis. Then the fields can be approximated by their asymptotic expansion (2.22). In particular, in this approximation the metric reads

$$ds^2 = \frac{1}{z^2} (dt^2 + (dx^1)^2 + (dx^2)^2 + dz^2) + \dots, \quad (3.10)$$

and admits a null radial geodesic with tangent vector $u = \partial_t + \partial_z$. For this particular geodesic we then have

$$T_{MN} u^M u^N = 2s\bar{s} + \dots = 2(1 - \eta^2)M^2 + \dots, \quad (3.11)$$

where in the last equality we have plugged in the definition of the sources for the \mathcal{PT} -broken phase (2.19). Hence, the above analysis tells us that, at least near the AdS boundary, the NEC is violated in the region where $|\eta| > 1$.

To determine whether this violation persists deep in the bulk we need to find an expression for the tangent vector of the radial null geodesics corresponding to our metric ansatz (2.17). However, as the metric components depend on the coordinate x^1 , we cannot find an analytic expression and we instead need to resort to a numerical approach for computing the geodesics.

Heuristically, what we do is numerically solve the trajectory of a massless particle in our background and then compute the tangent vector u . Numerically, we find that it is helpful to use z as the parameter of the trajectory. Moreover, we find that it is convenient to consider the reduced interval $\{\epsilon, 1 - \epsilon\}$ where ϵ is a small cutoff. The geodesic equations in terms of z then read

$$\ddot{y}^\mu + \Gamma^\mu_{MN} \dot{y}^M \dot{y}^N - \dot{y}^\mu \Gamma^z_{MN} \dot{y}^M \dot{y}^N = 0, \quad (3.12)$$

where μ denotes a boundary coordinate ($y^\mu = \{t, x^1, x^2\}$), M, N represent bulk coordinates ($y^M = \{t, x^1, x^2, z\}$) and the dot denotes derivatives with respect to z .

To obtain null radial geodesics such that near the AdS boundary $u \approx \partial_t + \partial_z$, we choose the following initial conditions

$$y^\mu(\epsilon) = \{0, x_0^1, 0\}, \quad \dot{y}^\mu(\epsilon) = \{\dot{t}_0, 0, 0\}, \quad (3.13)$$

where \dot{t}_0 is the positive root of the equation $g_{MN}(x_0^1, \epsilon) \dot{y}^M(\epsilon) \dot{y}^N(\epsilon) = 0$. It is worth noting that the equations of motion of x^2 decouple and thus we get $x^2(z) = 0$ for all z .

With this, we can solve numerically the geodesic equation (3.12) to obtain the tangent vector u given by

$$u = \dot{y}^\mu \partial_\mu + \partial_z. \quad (3.14)$$

This then allows us to compute the contraction $T_{MN} u^M u^N$ and thus to test the NEC for a given radial geodesic. We repeat this process for different values of x_0^1 to obtain a complete foliation of the spacetime.

In figure 12 we plot the final result for two \mathcal{PT} -broken solutions, a stable one with $\{a, T/M\} = \{1.7, 0.5\}$ and an unstable one with $\{a, T/M\} = \{1.9, 0.5\}$. We observe that the “degree of violation” of the NEC decreases towards the horizon. This is in stark contrast with [20], where for time-dependent sources the NEC was violated only deep in the bulk. As we shall see in the next section, our observed behaviour seems to be closely related to the fact that the geometry becomes homogeneous deep in the IR. In [19] the authors found that the NEC is generically violated everywhere in the bulk only for homogeneous solutions with $|\eta| > 1$; hence, as our homogeneous limit corresponds to $\eta = 0$, we expect the NEC to be preserved towards the IR of the theory. Thus to interpolate continuously between the UV violation and the IR preservation, one expects the “degree of violation” of the NEC to decrease as we indeed observe.

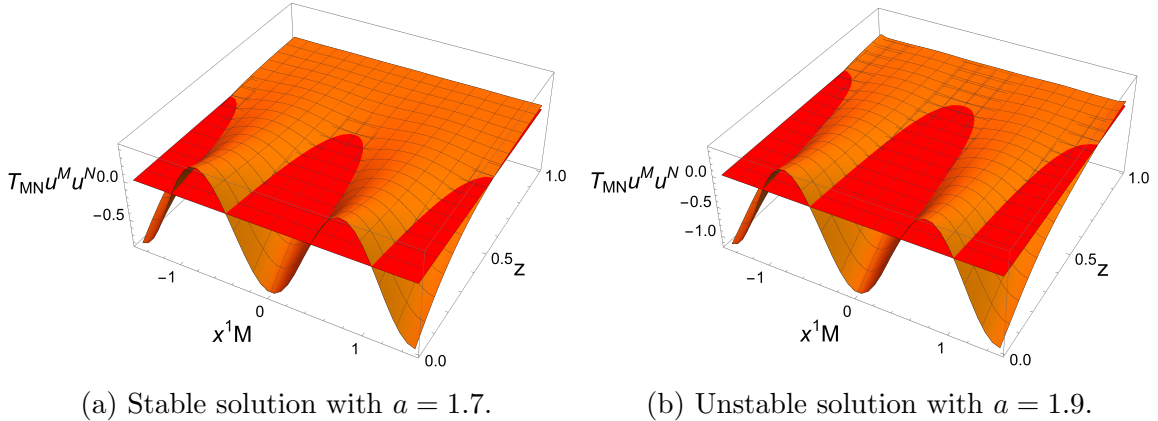


Figure 12: Violation of the NEC for the \mathcal{PT} -broken solutions at $T/M = 0.5$. The orange surface denotes $T_{MN}u^M u^N$ and the red one is the surface $T_{MN}u^M u^N = 0$ for reference.

Perhaps most remarkably, we find that both stable and unstable solutions have a very similar profile for $T_{MN}u^M u^N$. This seems to suggest that a priori one cannot determine the stability of the solution with knowledge of the violation of the NEC. This contrasts with the homogeneous setup where solutions that violated the NEC were also found to always be unstable [18, 19].

An interesting conclusion of the violation of the NEC is that the standard a -function [23–25], defined to be monotonically decreasing towards the IR, increases near the boundary. To prove this we proceed perturbatively in z .

Using the near-boundary expansion (2.22), we write the metric as

$$ds^2 = \frac{(1 - \delta(x^1)z^2)}{z^2} [-dt^2 + (dx^1)^2 + (dx^2)^2] + \frac{dz^2}{z^2} + \dots, \quad (3.15)$$

where the ellipsis denotes terms of order z and we have defined $\delta = s\bar{s}/4$. In order to define the a -function we introduce the domain wall coordinate

$$\rho = -\log(z) + \dots, \quad (3.16)$$

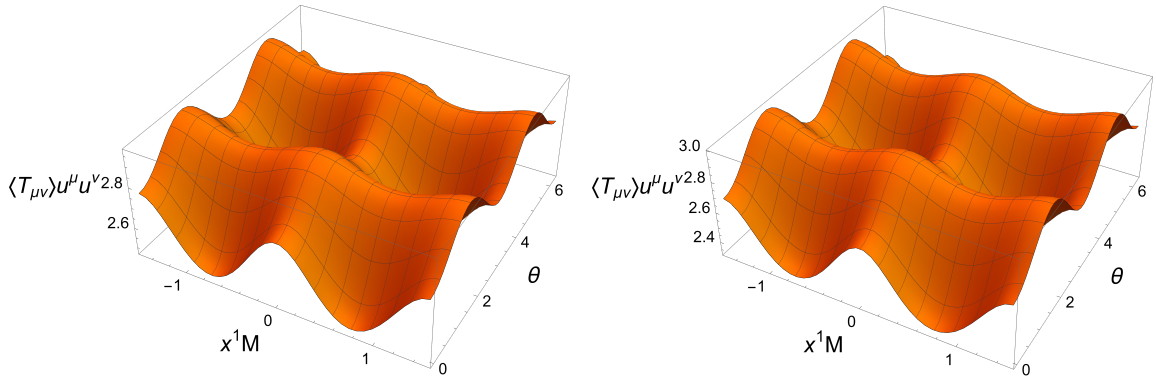
where now the ellipsis denotes terms of order z^3 . When written in terms of this radial coordinate ρ , the metric (3.15) takes the standard domain wall form

$$ds^2 = e^{2A} [-dt^2 + (dx^1)^2 + (dx^2)^2] + d\rho^2 + \dots, \quad A = \frac{1}{2} \log\left(\frac{1 - \delta z^2}{z^2}\right). \quad (3.17)$$

Then, using the definition of the a -function of [23–25] we get

$$a = \frac{\pi^{3/2}}{\Gamma(3/2)l_p^2} (\partial_\rho A)^{-2} = \frac{\pi^{3/2}}{\Gamma(3/2)l_p^2} (1 - \delta z^2)^2 = \frac{\pi^{3/2}}{\Gamma(3/2)l_p^2} \left(1 - \frac{s\bar{s}}{4} z^2\right)^2, \quad (3.18)$$

where l_p is the Planck length. Remarkably, a increases towards $z > 0$ for $s\bar{s} < 0$, i.e., for $|\eta| > 1$. Therefore, we find that for lattices with a non-Hermitian function



(a) Stable solution with $a = 1.7$.

(b) Unstable solution with $a = 1.9$.

Figure 13: Boundary NEC for the \mathcal{PT} -broken solutions at $T/M = 0.5$. The orange surface denotes $\langle T_{\mu\nu} \rangle u^\mu u^\nu$ where here the (boundary) null vector is $u = \partial_t + \cos(\theta)\partial_1 + \sin(\theta)\partial_2$. Remarkably for both stable and unstable solutions the boundary NEC is not violated.

η that locally satisfies $|\eta| > 1$, near the boundary, the a -function increases towards the IR. Hence, given that the a -function counts the degrees of freedom along the renormalization group (RG) flow, it seems that such lattices are problematic as after integrating out the UV, we (locally) gain degrees of freedom. Furthermore, defining the averaged a -function a_{av} as ⁷

$$a_{\text{av}} = \frac{\int_{-L/2}^{L/2} dx^1 \sqrt{g_{11}} a}{\int_{-L/2}^{L/2} dx^1 \sqrt{g_{11}}} = 1 - \frac{z^2}{2L} \int_{-L/2}^{L/2} dx^1 s \bar{s}, \quad (3.19)$$

we conclude that lattices with amplitudes greater than 2, globally gain degrees of freedom.⁸ However, one should note that the failure of the above a -functions to be monotonically decreasing is not enough to prove the previous assessments. In particular, to ensure that indeed we gain degrees of freedom along the RG flow, we would need to prove the non-existence of a monotonically decreasing function behaving as the central charge for $z \rightarrow 0$.

Lastly, we want to stress that despite the UV violation of the NEC, we have managed to find solutions that are seemingly stable at the linear level and which do not violate the boundary NEC (see figure 13). However, one should note that our stability analysis is not fully conclusive. Concretely, it can only find unstable QNMs crossing to the upper half of the complex plane near $\text{Re } \omega = 0$. Hence, if there were unstable modes crossing with $|\text{Re } \omega| \gg 1$, we would be insensitive to them.

⁷We thank K. Landsteiner for suggesting the inclusion of this computation.

⁸Although we have not presented stable lattices with amplitudes $a > 2$ in this paper, we expect them to exist for high enough temperatures.

Moreover, due to our ansatz we are also incapable of detecting modes crossing with non-zero momentum in the x^2 direction.⁹

3.5 Low-temperature behaviour

In this section we look into the low-temperature behavior of the non-Hermitian lattice. As we describe next we observe that our geometry becomes homogeneous in the $T \rightarrow 0$ limit. This will allow us to construct the dual of the ground state of the non-Hermitian lattice. It is given by an inhomogeneous domain wall between two homogeneous AdS geometries and it implies that the IR of the $T = 0$ lattice corresponds to a \mathcal{PT} -unbroken state that can be mapped via a complexified $U(1)$ transformation (2.13) to the ground state of the homogeneous Hermitian system.

We study the low-temperature limit of the non-Hermitian lattice by computing numerical solutions at fixed $LM = 251.3$ and $a = 0.1$. We further set $q = 2$.¹⁰ We find that these choices are better suited for the numerics of this section. At the lowest temperatures we employ a Chebyshev grid with 220 points along the z direction and a Fourier grid with 30 points along the x^1 periodic direction. As illustrated by Fig. 14 we find that as T is lowered the near-horizon geometry becomes less inhomogeneous. In order to further characterize the IR geometry it is useful to recall that the zero temperature solution of the Hermitian theory features an IR fixed point given by

$$h_1 = h_2 = h_3 = h_4 = \frac{3v}{1+3v}, \quad h_5 = 0, \quad \phi = \bar{\phi} = \sqrt{\frac{2}{v}}, \quad A_1 = 0, \quad (3.20)$$

which corresponds to an AdS_{3+1} metric with $R = -12 - 4/v$. In the left panel of Fig. 14 we plot the standard deviation of the Ricci scalar at the horizon as a function of temperature. It is clear that the spatial dependence is washed away as temperature is lowered. Below $T/M \approx 0.002$, the standard deviation of the Ricci scalar at the horizon is $O(10^{-8})$ and thus the Ricci scalar at the horizon is homogeneous within our numerical precision. Moreover, one can actually check that all metric functions tend to the homogeneous solution above. We next plot the spatial average of the Ricci scalar along the bulk in the right panel of Fig. 14. One can see that at low enough temperature the near-horizon geometry corresponds to the fixed point (3.20). The dual geometry is then a domain wall interpolating between two homogeneous AdS spaces.

By examining the matter sector of the system one finds that the IR of the low-temperature solution of the non-Hermitian lattice is not exactly (3.20). As shown

⁹Given the magnitude of the gap observed in figure 10 for values of a sufficiently below a_{\max} (but above 1) one can reasonably expect that, if they occurred at all, these instabilities would happen only for sizable values of the momentum in the homogeneous spatial direction.

¹⁰It was noted in [33] that in order to have a conformal IR fixed point $q > 1/(L_{\text{IR}} \phi_{\text{IR}})$, where L_{IR} is the radius of the AdS IR geometry and ϕ_{IR} the IR value of the scalar field. For our setup this means $q > \sqrt{(1+3v)/6} \approx 1.29$ since $v = 3$.

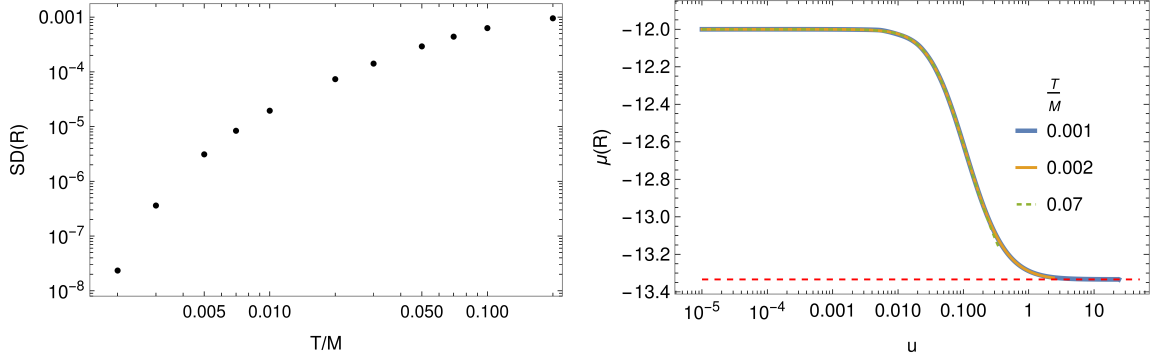


Figure 14: Left: standard deviation of the Ricci scalar at the horizon as a function of T/M . Right: spatial average of the Ricci scalar as a function of the radial coordinate $u = zM/M_0$, where $M_0 = 10$ is the value of the source for the $T = 0$ solution of section 3.5.1. The red dashed line indicates the value $R = -12 - 4/v$ corresponding to the IR fixed point (3.20).

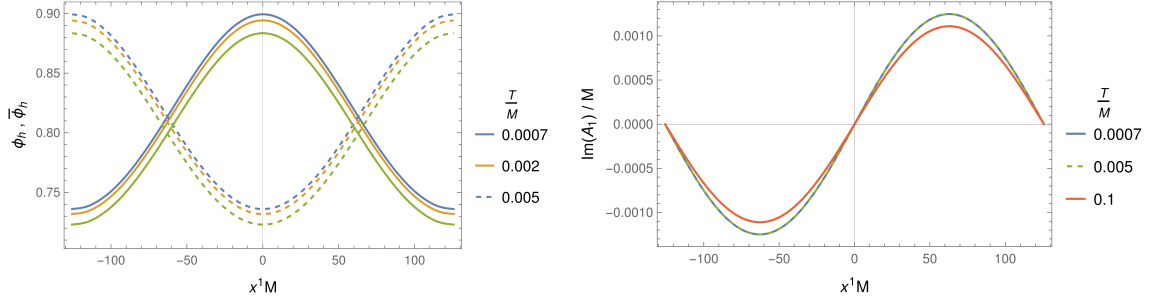


Figure 15: Left: ϕ (solid lines) and $\bar{\phi}$ (dashed lines) at the horizon for three different temperatures. Right: imaginary part of A_1 at the horizon. For temperatures below $T/M \approx 0.02$ plots of A_1 are indistinguishable from each other hence we also included the line for $T/M = 0.1$.

in Fig. 15, when T is lowered the matter fields ϕ , $\bar{\phi}$, and A_1 tend to inhomogeneous functions. We will see that in the $T \rightarrow 0$ limit these are a complexified $U(1)$ rotation (2.13) of the homogeneous solution (3.20). Therefore, our IR is the low energy counterpart of the UV configuration of case B in section 2.3. The geometry becomes that of AdS_{3+1} and the matter fields asymptote to a configuration as in (2.20), namely

$$\phi(1, x^1) = S\sqrt{\frac{2}{v}}, \quad \bar{\phi}(1, x^1) = S^{-1}\sqrt{\frac{2}{v}}, \quad A_1(1, x^1) = -\frac{i}{q}S^{-1}\partial_1 S, \quad (3.21)$$

with

$$S = \sqrt{\frac{1 - \tilde{\eta}}{1 + \tilde{\eta}}}, \quad (3.22)$$

where $\tilde{\eta} = \tilde{\eta}(x^1)$ is a function we can read from our numerical solutions.

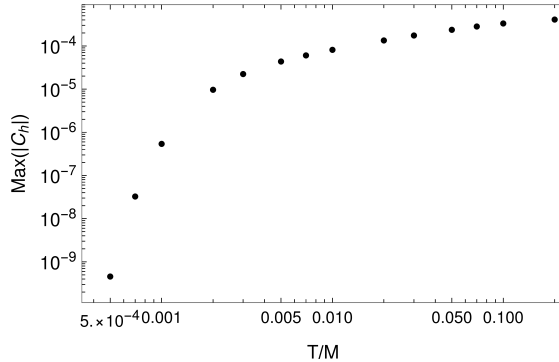


Figure 16: Plot of the IR constraint equation (3.23). We have defined $C = A_x - i(\phi \partial_1 \bar{\phi} - \bar{\phi} \partial_1 \phi)/(2q\phi\bar{\phi})$ and here we plot the maximum of its absolute value at the horizon.

In order to verify that the low-temperature IR of the system indeed obeys (3.21) one can check that the constraint

$$A_1|_{z=1} = i \frac{\phi \partial_1 \bar{\phi} - \bar{\phi} \partial_1 \phi}{2q\phi\bar{\phi}} \Big|_{z=1}, \quad (3.23)$$

which follows readily from (3.21),¹¹ is satisfied in the IR of our solution. We plot this constraint in Fig 16 where one can check that indeed it holds in the $T \rightarrow 0$ limit. It would then be interesting to determine the function $\tilde{\eta}$ characterizing the IR of our solutions and compare it to the function $\eta(x^1)$ that sets the UV non-Hermitian deformation. We will do that in the next subsection after constructing solutions at zero temperature.

3.5.1 The zero temperature solution

The features of the low-temperature solution hint at the existence of a zero temperature geometry given by a domain wall between two AdS fixed points. To look for zero temperature non-Hermitian lattices we follow [34] and adopt the metric ansatz

$$ds^2 = \frac{(z-1)^2}{z^2} \left[-h_1 dt^2 + h_3 (dx^1 + h_5 dz)^2 + h_4 (dx^2)^2 + \frac{h_2}{(z-1)^4} dz^2 \right], \quad (3.24)$$

where h_1, h_2, h_3, h_4, h_5 are functions of z and x^1 . As in the finite temperature ansatz we also switch on the matter fields $\phi, \bar{\phi}$ and A_1 as functions of z and x^1 .

We look for numerical solutions of the equations of motion (2.15) with the same UV boundary conditions (2.18). As in the low-temperature solutions above, we set $LM = 251.3$ and the amplitude of the non-Hermitian lattice to $a = 0.1$. Again we apply the DeTurck trick and modify the Einstein equations as discussed in section 3.1. In the IR we require the metric (3.24) to describe a zero temperature horizon

¹¹Notice that $\log(S^2) = \log(\phi/\bar{\phi})$, and thus one has that $A_1 = -i/(2q) \partial_1 \log(\phi/\bar{\phi})$.

and thus fulfill $h_5(1, x) = 0$, while the remaining metric functions are nonvanishing and, moreover, $h_1(1, x) = h_2(1, x)$ [34].

In our numerical simulations we set an IR cutoff at $z_{IR} = 1 - 10^{-3}$ and check that our solution at that cutoff approaches that of a zero temperature horizon.¹² We find that $|h_5(z_{IR}, x)| \leq 10^{-12}$ while all the remaining metric functions have converged to their values at the fixed point (3.20) within 5 significant digits. Our solutions satisfy the Maxwell constraint equation to $O(10^{-8})$. We have run these zero temperature numerical simulations employing a Chebyshev grid with 80 points for the z direction and a Fourier grid with 20 points for the x^1 direction. An extra subtlety is that due to the non-analytic behavior expected towards the IR we employ a fourth order finite-difference discretization along the z direction.

In the left panel of Fig. 17 we plot the spatial average of the Ricci scalar, $\mu(R)$, as a function of the radial coordinate for our zero temperature geometry. One can see that the scalar curvature indeed interpolates between the values corresponding to the UV and IR AdS fixed points. We have superimposed the result for $\mu(R)$ at a very low finite temperature to show that indeed the finite temperature geometry converges to the zero temperature domain wall in the $T \rightarrow 0$ limit. Our geometry is of course inhomogeneous inside the bulk, but the spatial dependence vanishes in the IR. To illustrate this, in the right panel of Fig. 17 we plot the standard deviation of R : it peaks at small values of the radial coordinate¹³ $u = z/(1 - z)$ and then quickly vanishes towards $u \rightarrow \infty$.

Next we check that the matter sector indeed realizes the IR fixed point (3.21). In the left panel of Fig. 18 we look at the spatial average of the product $\phi\bar{\phi}$. Notice that if (3.21) holds, $\sqrt{\phi\bar{\phi}} = \sqrt{2/v}$ in the IR, and, of course, the spatial averaging becomes superfluous there. Our numerics confirm that this is the case in the IR of the geometry. In the right panel of Fig 18 we show the gauge field A_1 at the horizon; it obeys the IR constraint (3.23). The matter sector is therefore realizing the \mathcal{PT} -unbroken fixed point (3.21), and we can now determine $\tilde{\eta}(x^1)$ from the IR of the zero temperature solution. Indeed, from (3.21) it follows that

$$\frac{\tilde{\eta}}{\sqrt{1 - \tilde{\eta}^2}} = \sqrt{\frac{v}{8}} (\bar{\phi} - \phi) \Big|_{z=1}. \quad (3.25)$$

In Fig. 19 we plot $\tilde{\eta}/\sqrt{1 - \tilde{\eta}^2}$ read from our numerical solution and compare it to the function $\eta(x^1)$ that defines the non-Hermitian UV sources. To numerical accuracy

¹²We checked that, as in [34], towards the IR the metric functions approach constant values but their derivatives are divergent. These divergences are ill-suited for our numerical methods and thus the need for an IR cutoff.

¹³This definition of the radial coordinate brings the metric ansatz (3.24) to a form that allows direct comparison with the finite temperature ansatz, in terms of $u = zM/M_0$, in the low T/M limit reached as $M \rightarrow \infty$.

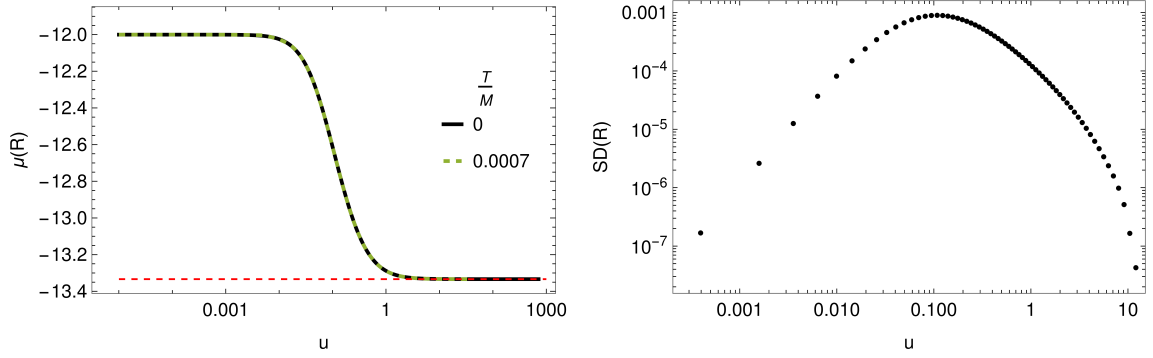


Figure 17: Left: spatial average of the Ricci scalar as a function of the radial coordinate for zero and very low temperature. The red dashed line indicates the value $R = -12 - 4v$ corresponding to the IR fixed point (3.20). Right: standard deviation of the Ricci scalar as a function of the radial coordinate for $T = 0$. Beyond $u \approx 10$, $SD(R)$ vanishes within our numerical precision. In both plots the radial coordinate is defined as $u = zM/M_0$ at finite T and $u = z/(1 - z)$ for $T = 0$.

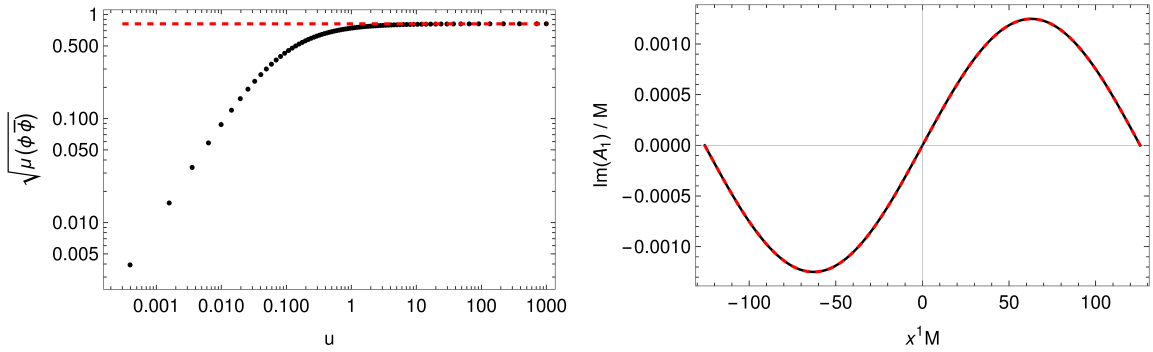


Figure 18: Left: square root of the spatial average of $\phi\bar{\phi}$ versus the radial coordinate. The red dashed line indicates the value $\sqrt{2/v}$ corresponding to the IR fixed point (3.20). Right: imaginary part of A_1 at the horizon. The solid black line shows the numerical solution for A_1 while the dashed red line results from solving for A_1 from the IR constraint (3.23).

we find the following relation tying $\tilde{\eta}(x^1)$ to $\eta(x^1)$:

$$\frac{\tilde{\eta}}{\sqrt{1 - \tilde{\eta}^2}} = \eta. \quad (3.26)$$

In summary, the zero temperature solutions confirm that the IR limit of our inhomogeneous non-Hermitian holographic theories is a \mathcal{PT} -unbroken fixed point. Our setup thus realizes an RG flow from an inhomogeneous \mathcal{PT} -broken non-Hermitian UV characterized by the source $\eta(x^1)$ to a pseudo-Hermitian IR resulting from a

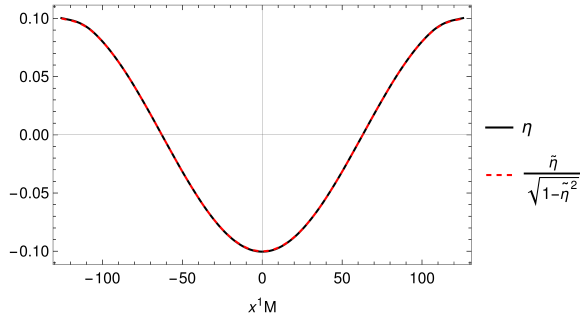


Figure 19: η (black solid line) and $\tilde{\eta}/\sqrt{1-\tilde{\eta}^2}$ (red dashed line).

complex $U(1)$ rotation, set by $\tilde{\eta}(x^1)$, of a homogeneous conformal fixed point.

4 Non-Hermitian junction

In section 3, we considered $\eta(x^1)$ to be a smooth periodic function. This was interpreted as constructing theories where the inflow/outflow is not highly localized, but rather smoothly extends throughout each site in a lattice.

It would also be interesting to explore a model where, rather than having inflow/outflow distributed across all sites in the lattice, we have a single cell where non-Hermiticities are present while the rest of the lattice is Hermitian (see figure 20 for a schematic). In this section we explore such a setup in the regime of spontaneous \mathcal{PT} -symmetry breaking characterized by the sources (2.19) with the following expression for $\eta(x^1)$

$$\eta(x^1) = \frac{a}{2 \tanh(\frac{L}{2\sigma})} \left[\tanh\left(\frac{x^1 + L/2}{\sigma}\right) - \tanh\left(\frac{x^1 - L/2}{\sigma}\right) \right], \quad (4.1)$$

where L is the width of the region where $\eta \neq 0$, a is the maximum and σ controls the steepness. We label this model *non-Hermitian Junction* due to its resemblance to a Josephson junction where instead of having superconductor/insulator/superconductor we now have Hermitian/non-Hermitian/Hermitian. Note that as σ and L are dimensional quantities, we can exploit the conformal symmetry of the UV to work in terms of their dimensionless equivalents σM and LM . Thus, solutions are parametrized by $\{a, T/M, LM, \sigma M, q\}$. For conciseness, we fix $q = 1$, $a = 0.7$, $T/M = 1$ and $LM = 3$; and we consider two junctions: a smooth one with $\sigma M = 1$ and a step one with $\sigma M = 0.2$. In figure 21 we plot $\eta(x^1)$ for these two junctions.

Regarding the numerical approach, we proceed exactly as in the previous sections, with only a few minor modifications. Instead of imposing periodic boundary conditions, we now consider $x^1 \in [-x_m^1, x_m^1]$, with x_m^1 such that $\partial_1 \eta(\pm x_m^1) \approx 0$; and impose that the x^1 -derivatives of all functions vanish on the boundaries $x^1 = \pm x_m^1$. Additionally, we use 4th order finite difference for the x^1 -derivatives instead of the

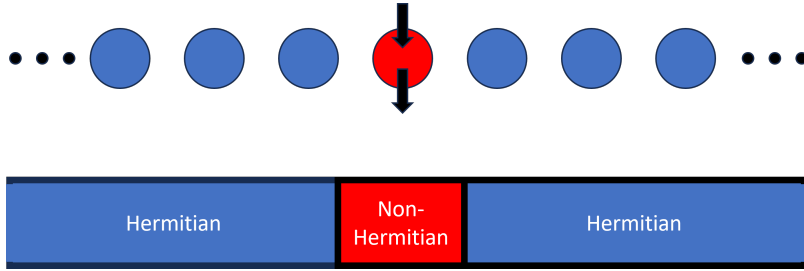


Figure 20: Schematic plot illustrating the construction of the non-Hermitian junction. (*Upper*) Lattice where in one of the sites (red circle) there is flow of matter from/to the exterior while in the remaining sites (blue circles) there is none. (*Lower*) As the lattice structure is broken by the existence of a special site, the lattice picture can be replaced by a junction consisting of a semi-infinite Hermitian system, a non-Hermitian system and another semi-infinite Hermitian system.

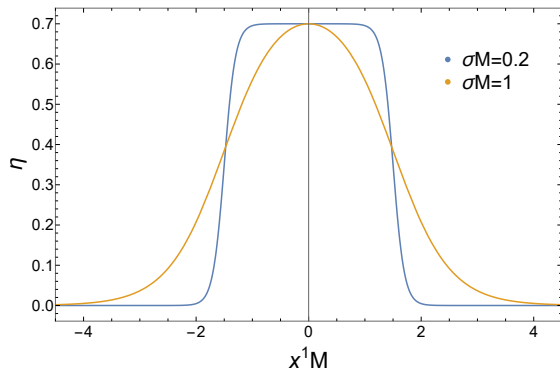


Figure 21: Non-Hermitian function $\eta(x^1)$ for the non-Hermitian junction.

Fourier derivative matrices that we have used previously. More explicitly, in the x^1 -direction we work with a 4th order finite difference grid with 250 points and in the z -direction we employ a Chebyshev-Gauss-Lobatto grid with 20 points.¹⁴ For the junctions with $\sigma M = 0.2$ and $\sigma M = 1$, we take $x_m^1 = 1.5L$ and $x_m^1 = 4L$, respectively.

In figures 22 and 23 we plot expectation values of the condensates $\langle \mathcal{O} \rangle$, $\langle \bar{\mathcal{O}} \rangle$, the current $\langle J_1 \rangle$ and the energy density $\langle T_{tt} \rangle$. As expected, the current (which we have argued was a feature of the inhomogeneous setup) vanishes in the regions where $\eta \approx \text{const}$. Moreover, we also find that the sign of the current matches the sign of $\partial_1 \eta$ (see figure 24). Hence, for \mathcal{PT} -invariant sources we expect the current to always be an odd function of x^1 . Together, these observations seem to indicate that, in general, in a non-Hermitian junction the current appears localized at the interfaces and that its integral vanishes. In particular, in the limit $\sigma \rightarrow 0$ we expect that the current becomes a pair of deltas of opposite sign localized at $x^1 = \pm L/2$.

¹⁴With this grid size the study of QNFs becomes unfeasible with our methods.

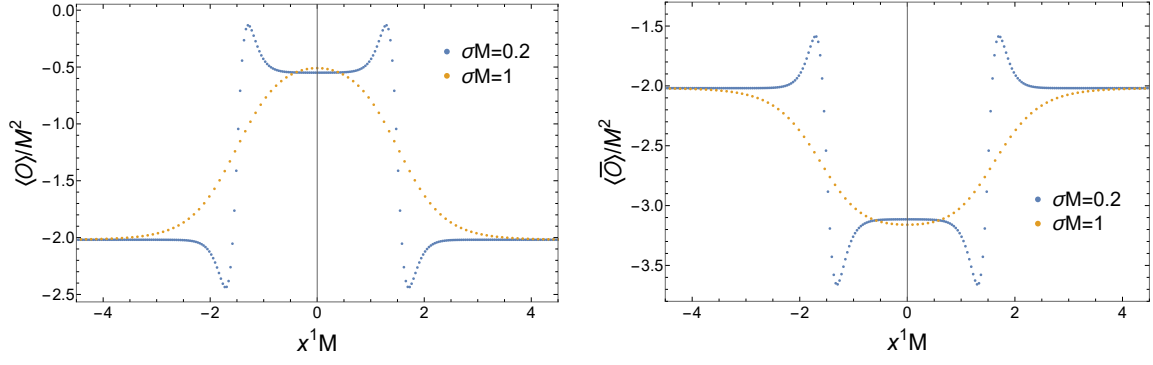


Figure 22: Expectation values of the condensates $\langle \mathcal{O} \rangle$ and $\langle \bar{\mathcal{O}} \rangle$ in the non-Hermitian junction.

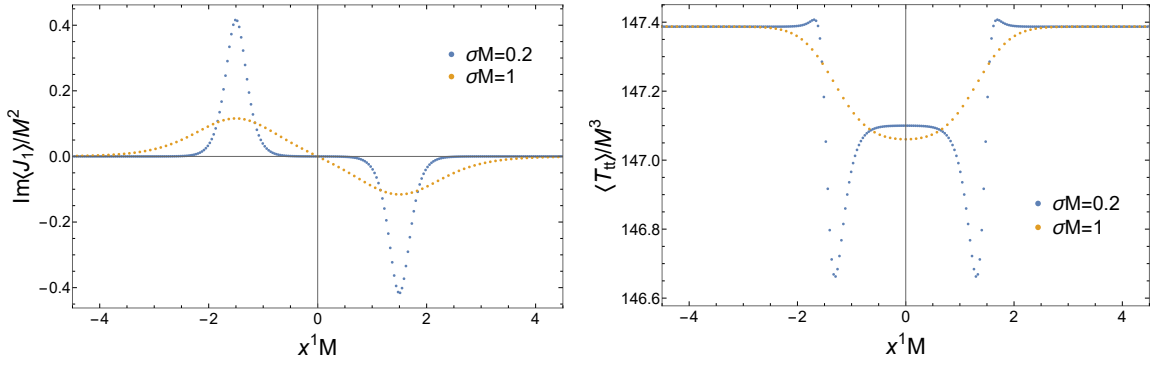


Figure 23: Expectation values of the current $\langle J_1 \rangle$ (left) and the energy density $\langle T_{tt} \rangle$ (right) for the non-Hermitian junction. We note that $\langle J_1 \rangle$ is purely imaginary.

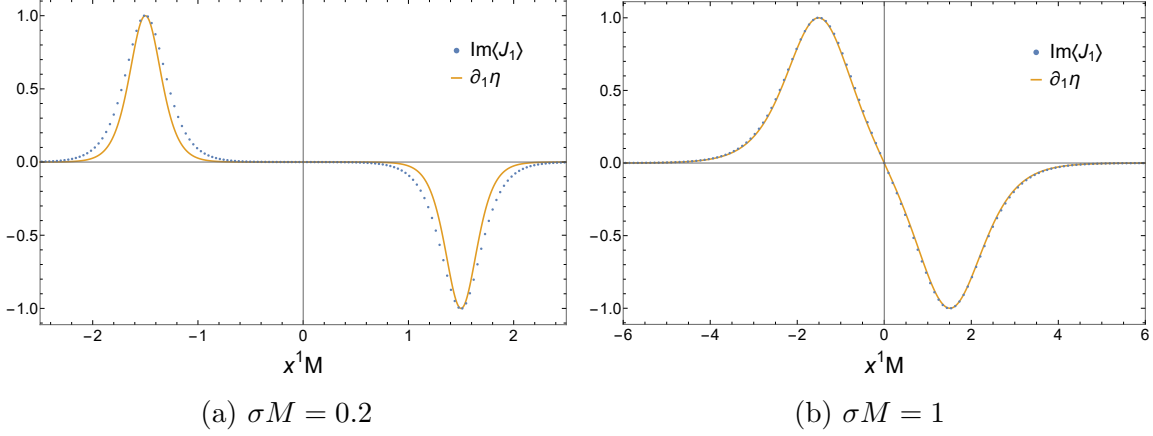


Figure 24: Comparison between the current $\langle J_1 \rangle$ and $\partial_1 \eta$. Both functions have been normalized so that their maximum is 1. Remarkably, the current appears only in the regions where $\partial_1 \eta \neq 0$ and has the same sign as $\partial_1 \eta$.

5 Conclusions

In this paper we have constructed \mathcal{PT} -symmetric inhomogeneous non-Hermitian models in holography. We have generalized the setup [18] to describe inhomogeneous systems and we have used it to study lattices where in each site there is some non-Hermiticity, as well as Hermitian/non-Hermitian/Hermitian junctions. We labelled the former setup *non-Hermitian lattice* and the latter *non-Hermitian junction*.

Following the construction of [18], we introduced the non-Hermiticity through the sources s and \bar{s} of an operator charged under a $U(1)$ symmetry. We parameterized this non-Hermiticity using $\eta(x^1)$ which, for our models, was given by the ratio

$$\eta = \frac{s - \bar{s}}{s + \bar{s}}. \quad (5.1)$$

We also allowed for solutions with a complex external gauge field a_μ . We distinguished between two cases, $a_1 = iq^{-1}\partial_1\eta/(1 - \eta^2)$ and $a_1 = 0$. For the former, we found that the Dyson map (2.11) could map the model to a Hermitian one, and we explicitly checked that indeed the dynamics allowed for an equivalent Hermitian description. This equivalence is physically non-trivial as the systems described by the Hermitian and non-Hermitian models are fundamentally very different: one has a complex external gauge field and inflow/outflow of matter while the other does not [20]. This suggests that one should think of the Dyson map as a duality between different theories. Hence although the dynamics are mathematically equivalent the physical interpretation is fundamentally different. An alternative interpretation where the Dyson map is considered a gauge symmetry can be found in [1, 12].

For models with $a_1 = 0$, we found that no Dyson map of the form (2.11) could bring them into a Hermitian description. Furthermore these models spontaneously break \mathcal{PT} by an emerging complex current localized in the region where $\partial_1\eta \neq 0$. Interestingly, as opposed to the \mathcal{PT} -broken solutions found in the homogeneous setup [18, 19], our solutions still have a real metric. The existence of spontaneous \mathcal{PT} -breaking suggests that these systems do not allow for unitary evolution. However, we lack a definitive answer to that question as there could be a different definition of \mathcal{PT} preserved by these solutions.

It was observed in [18, 19] that in the case of constant η , the dual geometry becomes unstable for $|\eta| > 1$. Nonetheless, here we have found stable \mathcal{PT} -breaking solutions with regions where $|\eta(x^1)| > 1$. However, near the AdS boundary, these solutions violate the null energy condition (NEC) and have an a -function that locally increases towards the IR. This seems to suggest that these solutions are problematic. In particular, as the a -function counts the number of degrees of freedom along the renormalization group flow, these solutions seemingly gain degrees of freedom after integrating out the UV. One should note however that this need not be the case. To prove that the number of degrees of freedom increases it is not sufficient to study

the standard a -function, we would have to show that no monotonically decreasing function behaving as the central charge exists.

We shall stress that despite the apparent issues, the \mathcal{PT} -breaking solutions with $|\eta(x^1)| > 1$ do not violate the boundary NEC. Moreover, our analysis of the quasinormal frequencies (QNFs) indicates that for $|\eta(x^1)|$ sufficiently small but larger than 1, these solutions are linearly stable. However, this analysis is not fully conclusive as it can only find unstable QNFs crossing to the upper half of the complex plane near $\text{Re}\omega = 0$. Hence, there could be unstable modes crossing onto the upper half plane at large values of $|\text{Re}\omega|$, which we would fail to observe. Furthermore, in our analysis we neglected the possibility of having momentum in the direction perpendicular to the inhomogeneities. Thus, there could also be instabilities arising from modes with non-zero momentum in that direction.

To further characterize the \mathcal{PT} -breaking solutions, we have also studied their low-temperature behaviour. This analysis has been restricted to $|\eta(x^1)| < 1$ due to limitations in the numerics. We have observed that the IR geometry corresponds to that of a Hermitian conformal fixed point rotated under a complexified $U(1)$. We thus elucidate that the IR geometry restores \mathcal{PT} , and indeed we showed that a Dyson map of the form (2.11) connects it to the Hermitian theory which is \mathcal{PT} -unbroken. Hence we claim that our \mathcal{PT} -broken solutions flow to a \mathcal{PT} -unbroken theory in the IR. We believe such behaviour is closely related to the irrelevant character of the inhomogeneities that introduced the \mathcal{PT} -breaking. Remarkably, the \mathcal{PT} -symmetry restoration observed in our strongly-coupled setting has also been found in the perturbative regime in [1]. It would be interesting to test whether this is a generic property of inhomogeneous non-Hermitian field theories. If this were to be the case, then perhaps one could try to identify some Hermitian field theories as the IR-fixed point of a non-Hermitian model in the UV; thus offering a new window onto the underlying structure of the former.

It is worth noting that many of the above results have been tested primarily in the non-Hermitian lattice. However, we expect them to also hold for the non-Hermitian junction. Regrettably numerical difficulties have prevented us from a thorough exploration of the latter model.

In this paper we have started the exploration of inhomogeneous non-Hermitian theories via holography. This work opens the way for several lines of research in the realm of strongly coupled non-Hermitian theories. We next list some of them.

- Determine the phase diagram of non-Hermitian lattices and junctions. In [19] the authors identified a rich phase structure for the homogeneous system and found a phase with complex metric that dominated at large $|\eta|$. It would be interesting to see if such phase exists for our inhomogeneous setup. This could provide new insights on the nature of the low-temperature \mathcal{PT} -breaking solutions, specially for $|\eta(x^1)| > 1$.

- Study transport properties of non-Hermitian lattices and junctions. It would be interesting to extend the study of transport properties of [19] to the inhomogeneous lattice.
- Study the non-Hermitian junction in greater detail. In this paper, we have limited our analysis of the junction to a proof-of-concept. It would be interesting to delve deeper into the phenomenology of these solutions and try to compare with realistic condensed matter systems.
- Study if IR \mathcal{PT} restoration is a general feature of other inhomogeneous systems. Considering that this phenomenon has been observed both in the perturbative [1] and non-perturbative limits, it would be interesting to study different strongly-coupled realizations of inhomogeneous non-Hermitian systems to assess whether this is a generic feature of non-Hermitian inhomogeneous QFTs.
- An interesting new direction would be that of the study of non-Hermitian deformations around quantum critical points. In [10] it was observed that a non-Hermitian lattice can qualitatively modify the dynamics about a quantum critical point. Via holography we can explore these effects on strongly coupled systems.

Acknowledgements

We thank J.L.F. Barbón, P.G. Romeu, and specially K. Landsteiner for valuable discussions. This work is supported through the grants CEX2020-001007-S and PID2021-123017NB-I00 funded by MCIN/AEI/10.13039/501100011033 and by ERDF “A way of making Europe”. The work of D.G.F. is supported by FPI grant PRE2022-101810. Some numerical simulations were carried out at the IFT Hydra cluster.

A Holographic dictionary

In this appendix, we follow the standard holographic renormalization procedure [35], to compute the one-point functions presented in equation (2.23).

We commence by first defining the renormalized action \mathcal{S}_{ren} associated with the bulk action (2.12)

$$\mathcal{S}_{ren} = \int d^4y \sqrt{-g} \left(R - 2\Lambda - \frac{1}{4} F_{MN} F^{MN} - \mathcal{D}_M \phi \mathcal{D}^M \bar{\phi} - m^2 \phi \bar{\phi} - \frac{v}{2} \phi^2 \bar{\phi}^2 \right) + \mathcal{S}_{ct}, \quad (\text{A.1})$$

where \mathcal{S}_{ct} is the standard counter-term (see e.g. [36])

$$\mathcal{S}_{ct} = \frac{1}{2} \int_{z=\epsilon} d^3x \sqrt{-\gamma} (2K - 4 - \phi \bar{\phi}) . \quad (\text{A.2})$$

Here, $\gamma_{\mu\nu}$ is the induced metric at the $z = \epsilon \rightarrow 0$ hypersurface and K is the trace of the extrinsic curvature $K_{\mu\nu}$

To compute one-point functions we need the variation of the renormalized action (A.1) evaluated on-shell, which yields

$$\begin{aligned} \delta S_{ren} = & -\frac{1}{2} \int_{z=\epsilon} d^3x \sqrt{-\gamma} \left(\frac{1}{2} \gamma_{\mu\nu} \phi \bar{\phi} + (K - 2) \gamma_{\mu\nu} - K_{\mu\nu} \right) \delta \gamma^{\mu\nu} \\ & - \frac{1}{2} \int_{z=\epsilon} d^3x \sqrt{-\gamma} \left(n_\alpha (\delta \phi \mathcal{D}^\alpha \bar{\phi} + \delta \bar{\phi} \mathcal{D}^\alpha \phi + \delta A_\mu F^{\alpha\mu}) - \bar{\phi} \delta \phi - \phi \delta \bar{\phi} \right), \end{aligned} \quad (\text{A.3})$$

where n_α is the outward-pointing unit normal vector corresponding to the $z = \epsilon$ boundary. Plugging in the asymptotic expansion (2.22) and redefining the fluctuations as

$$\delta \gamma^{\mu\nu} = \delta \gamma_{(b)}^{\mu\nu} z^{-2}, \quad \delta A_\mu = \delta A_\mu^{(b)}, \quad \delta \phi = \delta \phi^{(b)} z, \quad \delta \bar{\phi} = \delta \bar{\phi}^{(b)} z, \quad (\text{A.4})$$

the above expression simplifies to

$$\begin{aligned} \delta S_{ren} = & \int_{z=\epsilon} d^3x \left(-1 - h_2^{(3)} - \frac{3}{2} (h_3^{(3)} + h_4^{(3)}) - \frac{1}{2} (s\bar{\phi}^{(2)} + \bar{s}\phi^{(2)}) \right) \delta \gamma_{(b)}^{tt} \\ & + \int_{z=\epsilon} d^3x \left(-\frac{1}{2} + h_2^{(3)} + \frac{3}{2} (h_1^{(3)} + h_4^{(3)}) + \frac{1}{2} (s\bar{\phi}^{(2)} + \bar{s}\phi^{(2)}) \right) \delta \gamma_{(b)}^{11} \\ & + \int_{z=\epsilon} d^3x \left(-\frac{1}{2} + h_2^{(3)} + \frac{3}{2} (h_1^{(3)} + h_3^{(3)}) + \frac{1}{2} (s\bar{\phi}^{(2)} + \bar{s}\phi^{(2)}) \right) \delta \gamma_{(b)}^{22} \\ & + \int_{z=\epsilon} d^3x \left(A_1^{(1)} \delta A_1 + \bar{\phi}^{(2)} \delta \phi^{(b)} + \phi^{(2)} \delta \bar{\phi}^{(b)} \right) + \text{terms of order } \epsilon \end{aligned} \quad (\text{A.5})$$

where we have introduced $h_2^{(3)} = -(h_1^{(3)} + h_3^{(3)} + h_4^{(3)})/3$. Finally, upon considering the usual holographic prescription for flat AdS boundaries

$$\langle T_{\mu\nu} \rangle = -2 \lim_{\epsilon \rightarrow 0} \frac{\delta \mathcal{S}_{ren}}{\delta \gamma_{(b)}^{\mu\nu}}, \quad \langle J^\mu \rangle = \lim_{\epsilon \rightarrow 0} \frac{\delta \mathcal{S}_{ren}}{\delta A_\mu^{(b)}}, \quad \langle \mathcal{O} \rangle = \lim_{\epsilon \rightarrow 0} \frac{\delta \mathcal{S}_{ren}}{\delta \bar{\phi}^{(b)}}, \quad \langle \bar{\mathcal{O}} \rangle = \lim_{\epsilon \rightarrow 0} \frac{\delta \mathcal{S}_{ren}}{\delta \phi^{(b)}}, \quad (\text{A.6})$$

we recover the one-point functions presented in equation (2.23).

B Further details on the computation of the QNFs

Here we describe in detail the setup used in the computation of the QNFs presented in section 3.3. We follow the approach of [37], generalizing it to a backreacted setup. The idea behind the method is to use coordinates regular at the horizon, so that ingoing boundary conditions become instead regularity conditions there; then write the equations of motion for the linearized fluctuations as a generalized eigenvalue problem

$$\hat{\mathcal{A}} \Phi = \omega \hat{\mathcal{B}} \Phi, \quad (\text{B.1})$$

where Φ is a multi-component field and $\hat{\mathcal{A}}, \hat{\mathcal{B}}$ differential operators; and finally discretize the system in a Chebyshev grid to obtain the eigenvalues numerically. Notably, for the computation of the eigenvalues, it is convenient to rewrite the discretized version of the generalized eigenvalue problem (B.1)

$$\mathcal{A}\Phi = \omega\mathcal{B}\Phi, \quad (\text{B.2})$$

where now \mathcal{A} and \mathcal{B} are matrices, as a standard eigenvalue problem by inverting \mathcal{B} , namely

$$\mathcal{Q}\Phi = \omega\Phi, \quad \mathcal{Q} = \mathcal{B}^{-1}\mathcal{A}. \quad (\text{B.3})$$

This in turn allows us to determine the lowest lying QNFs using Arnoldi iteration, which significantly speeds up the computation (see e.g. chapter 28 of [38]).

To better illustrate the numerical method, in subsection B.1 we consider the probe limit of the setup presented in section 3. After discussing the approach in that toy model, in subsection B.2 we explain how to generalize the method to the backreacted setup.

B.1 Toy model: Probe limit

In the probe limit the Einstein Hilbert part of the action (2.12) drops, and we consider the metric fixed to be SAdS₃₊₁ in regular coordinates [39, 40] (these are the AdS equivalent of the hyperboloidal slicing frequently used in asymptotically flat spacetimes, see for instance [41–43] for a recent overview)

$$ds^2 = \frac{1}{z^2} [-(1-z^3)dt^2 + (dx^1)^2 + (dx^2)^2 + (1+z^3)dz^2 - 2z^3 dt dz]. \quad (\text{B.4})$$

Notably, with this choice of coordinates imposing infalling boundary conditions for the QNMs corresponds to demanding regularity at the horizon $z = 1$. Alternatively, one could consider the metric written in ingoing Eddington-Finkelstein coordinates, which simplifies the computation of the QNFs significantly. However, when considering backreaction of the metric, we found that it was more convenient to implement regular-like coordinates as they allowed for an invertible \mathcal{B} matrix in the discretized eigenvalue equation (B.2). Hence, in this section we consider regular coordinates to better connect with the upcoming discussion of the backreacted case.

To study the QNMs we consider the following ansatz for the fields ϕ and A_M

$$\phi = \phi^{(bg)}(x^1, z) + z\delta\phi(x^1, z)e^{-i\omega t + ikx^1}, \quad (\text{B.5a})$$

$$\bar{\phi} = \bar{\phi}^{(bg)}(x^1, z) + z\delta\bar{\phi}(x^1, z)e^{-i\omega t + ikx^1}, \quad (\text{B.5b})$$

$$A = A_1^{(bg)}(x^1, z)dx^1 + \delta A_\mu(x^1, z)e^{-i\omega t + ikx^1}dx^\mu, \quad (\text{B.5c})$$

where all functions are regular at the horizon $z = 1$. The terms with the superscript (bg) correspond to the background solution and thus satisfy the boundary conditions

$$\partial_z\phi^{(bg)}(x^1, 0) = s(x^1), \quad \partial_z\bar{\phi}^{(bg)}(x^1, 0) = \bar{s}(x^1), \quad A_1^{(bg)}(x^1, 0) = a_1(x^1), \quad (\text{B.6})$$

and $\{\delta\phi, \delta\bar{\phi}, A_\mu\}$ are linearized fluctuations that represent the quasinormal modes and thus satisfy Dirichlet boundary conditions at $z = 0$

$$\delta\phi(x^1, 0) = \delta\bar{\phi}(x^1, 0) = \delta A_\mu(x^1, 0) = 0. \quad (\text{B.7})$$

Here we focus on the non-Hermitian lattice introduced in section 3 in the \mathcal{PT} -breaking phase (see section 3.2.1) with lattice constant $LM = 6$ and scalar charge $q = 1$.¹⁵ Hence, due to conformal invariance of the UV theory, solutions are characterized by only two background parameters $\{a, T/M\}$; and the momentum k/M .

As discussed in section 3.3 fluctuations can be decoupled into two sectors according to their transformation under reflections along the x^2 axis

- i. Odd: $\{\delta A_2\}$.
- ii. Even: $\{\delta\phi, \delta\bar{\phi}, \delta A_t, \delta A_1\}$.

We consider only the even sector, as it is the more interesting for presentation of the method. Then, the equations of motion for the fluctuations are

$$\delta [\nabla_M F^M_t + iq (\phi \mathcal{D}_t \bar{\phi} - \bar{\phi} \mathcal{D}_t \phi)] = 0, \quad (\text{B.8a})$$

$$\delta [\nabla_M F^M_1 + iq (\phi \mathcal{D}_1 \bar{\phi} - \bar{\phi} \mathcal{D}_1 \phi)] = 0, \quad (\text{B.8b})$$

$$\delta [(\nabla_M - iq A_M) \mathcal{D}^M \phi + m^2 \phi + v \phi^2 \bar{\phi}] = 0, \quad (\text{B.8c})$$

$$\delta [(\nabla_M + iq A_M) \mathcal{D}^M \bar{\phi} + m^2 \bar{\phi} + v \bar{\phi}^2 \phi] = 0, \quad (\text{B.8d})$$

$$\delta [\nabla_M F^M_z + iq (\phi \mathcal{D}_z \bar{\phi} - \bar{\phi} \mathcal{D}_z \phi)] = 0, \quad (\text{B.8e})$$

where the δ indicates that in the equation we consider only the linear term in the fluctuations. We have a total of 5 equations for 4 fields. These equations however are linearly dependent and one can build a set of 4 linearly independent equations that, when satisfied, imply the original 5 equations. In the usual approach one would try to construct this set of 4 equations. However, there is also a more brute-forced alternative: we could choose any independent set of 4 equations not necessarily implying the remaining one, solve them, and then discard the solutions that do not satisfy the remaining equation. To illustrate this, consider the following example. Let us have a system of two differential equations

$$y''(x) + \lambda y'(x) = 0, \quad y'(x) + \lambda y(x) = 0. \quad (\text{B.9})$$

To solve this system, we note that satisfying the second equation implies satisfying the first as they are related by derivation. Hence the system can be reduced to solving only the second equation, finding that

$$y(x) = c_1 e^{-\lambda x}. \quad (\text{B.10})$$

¹⁵Note that in the main text we have used $LM = 3$ in the computation of the QNFs.

Alternatively, we could simply choose one of the equations at random, solve it and then check whether the other one is satisfied. Let us choose the first one, the solutions are

$$y(x) = c_2 + c_1 e^{-\lambda x}, \quad (\text{B.11})$$

then we see that in order to also be a solution to the second equation, all solutions with $c_2 \neq 0$ should be discarded.

The main takeaway here is any independent set of equations from (B.8) must necessarily contain all solutions to the system plus potentially some unphysical solutions that play the role of the $c_2 \neq 0$ solutions in (B.11). Hence, instead of trying to find the minimal set of independent equations that imply (B.8), we opt for the simpler, although less elegant, approach of selecting some set of equations; computing the eigenvalues and eigenfunctions and then discarding those eigenvalues that are unphysical as they do not satisfy the remaining equations.¹⁶

In practice, we do not choose the independent equations at random. Instead, we choose a set that is conveniently suited for our numerical implementation by demanding that the \mathcal{B} matrix in (B.2) is invertible and that only a few of the unphysical quasinormal frequencies appear near the origin of the complex plane. We found that an adequate choice was taking equations (B.8a)-(B.8d). It is important to note that, as the aforementioned set of equations is quadratic in ω , we need to introduce auxiliary fields

$$\{\delta \tilde{A}_1, \delta \tilde{\phi}, \delta \tilde{\phi}^{\bar{}}\} = -i\omega \{\delta A_1, \delta \phi, \delta \bar{\phi}\}, \quad (\text{B.12})$$

to be able to write a generalized eigenvalue problem.

Before moving on to the discussion of the numerical implementation, let us comment on two relevant issues. Firstly, the existence of more equations of motion than fields is a byproduct of fixing gauge. For any given sector, we always have as many equations as components before gauge fixing. Hence for the odd sector we need not worry about all the issues discussed above. Secondly, we want to stress that we can consistently impose Dirichlet boundary conditions instead of gauge-invariant boundary conditions. The key realization is that, after radial gauge fixing, imposing regularity on the horizon does not fix the remaining gauge invariance and hence we are free to impose Dirichlet boundary conditions on the boundary of AdS. Once we have fixed the radial gauge, the remaining residual gauge transformations cannot

¹⁶Note that our approach could fail in the presence of degenerate eigenvalues. Say two eigenvectors φ_1 and φ_2 are solutions to the chosen equations with eigenvalue ω . Then we could have that only some combination $\alpha\varphi_1 + \beta\varphi_2$ satisfies the constraint while φ_1 and φ_2 independently do not satisfy it. In practice, within our setup, such possibility leads to no relevant issues. We make sure that indeed we are not losing information by checking that the QNFs we find continuously connect with those obtained in the homogeneous $\eta = 0$ case; which we can compute without using the brute-forced approach.

take us away from the regular solutions as they have to be z -independent.¹⁷ Hence, we can use a gauge transformation to shift any solution to satisfy Dirichlet boundary conditions.

Regarding the numerics, we first place the system in a lattice, for the z -direction we consider a Chebyshev-Lobatto grid and for the x^1 -direction, which is periodic with period L , we take an equispaced grid. This in turn, allows us to discretize the relevant differential operators using Chebyshev and Fourier differentiation matrices to replace ∂_z and ∂_1 , respectively. With this, we first solve for the background as indicated in section 3.1 and then construct the \mathcal{A} and \mathcal{B} matrices corresponding to the discretization of the generalized eigenvalue problem arising from equations (B.8a)-(B.8d). Once these matrices are constructed, we compute $\mathcal{Q} = \mathcal{B}^{-1}\mathcal{A}$ and obtain a small set of low-lying eigenvalues and eigenvectors using Arnoldi iteration. We then construct the discretized version of the remaining equation (B.8e) and select only those eigenvalues whose eigenvectors satisfy it with a certain tolerance.

To give an explicit example, in table 1 we present the QNFs computed for $\{a, T/M\} = \{0.4, 1\}$ at momentum $k/M = \frac{4\pi}{3} \cdot 10^{-4}$.¹⁸ We have employed a lattice with $N_1 \times N_z = 16 \times 20$ sites and a tolerance of 10^{-8} . In order to locate the shown QNFs we have obtained a total of 20 eigenvalues and eigenvectors of \mathcal{Q} . Remarkably, due to the spectral instability observed in [40] the numerical round-off errors arising from the inversion of \mathcal{B} caused the eigenvalues to migrate significantly. To avoid this issue, we found that it was sufficient to artificially¹⁹ increase the numerical precision to $5 \times \text{MachinePrecision}$ when computing the eigenvalues. Interestingly we found that the numerical error associated to the background was negligible for the low-lying QNFs.

B.2 Adding backreaction

Now that the general approach has been introduced in the probe limit, we can proceed to add backreaction. However we wish to consider the background metric in regular-like coordinates as they were essential in the construction of the previous section.

¹⁷After fixing radial gauge, the residual gauge transformations are large gauge transformations by construction.

¹⁸Notably, taking $k/M \neq 0$ seems to improve the quality of the numerics specially when adding backreaction. For that reason we choose to always work at small but nonzero k/M .

¹⁹Background solutions are computed with MachinePrecision and then promoted to data with $5 \times \text{MachinePrecision}$.

Re(ω)	Im(ω)
0	-0.0479634
± 0.996619	-0.578461
± 0.996174	-0.579758
0	-1.62071
± 1.27715	-1.52475
± 1.35876	-1.54718
± 2.09013	-0.467175
± 2.09033	-0.467161
± 1.72459	-1.46457
± 1.72859	-1.4667
± 1.77647	-1.47722

Table 1: QNFs for $\{a, T/M\} = \{0.4, 1\}$ at $k/M = \frac{4\pi}{3} \cdot 10^{-4}$.

For that reason we take the following ansatz

$$ds^2 = g_{MN}^{(bg)}(x^1, z) dx^M dx^N + \frac{1}{z^2} \delta g_{\mu\nu}(x^1, z) e^{-i\omega t + ikx^1} dx^\mu dx^\nu, \quad (\text{B.13a})$$

$$\phi = \phi^{(bg)}(x^1, z) + z \delta \phi(x^1, z) e^{-i\omega t + ikx^1}, \quad (\text{B.13b})$$

$$\bar{\phi} = \bar{\phi}^{(bg)}(x^1, z) + z \delta \bar{\phi}(x^1, z) e^{-i\omega t + ikx^1}, \quad (\text{B.13c})$$

$$A = A_1^{(bg)}(x^1, z) dx^1 + \delta A_\mu(x^1, z) e^{-i\omega t + ikx^1} dx^\mu, \quad (\text{B.13d})$$

where the background metric $g_{MN}^{(bg)}(x^1, z)$ is written in a regular-like ansatz

$$g_{MN}^{(bg)} dx^M dx^N = \frac{1}{z^2} \left[- (1 - z^3) h_1 dt^2 + h_3 (dx^1 + 2h_5 dz)^2 + h_4 (dx^2)^2 \right. \\ \left. + (1 + z^3) h_2 dz^2 - 2z^3 h_6 dt dz + 2h_7 dt dx \right], \quad (\text{B.14})$$

with $h_i = h_i(x^1, z)$. We demand regularity of all the functions at the horizon $z = 1$ and at $z = 0$ we require that the background satisfies

$$g_{MN}^{(bg)}(x^1, 0) dx^M dx^N = \frac{1}{z^2} \left[-dt^2 + (dx^1)^2 + (dx^2)^2 + dz^2 \right], \\ \partial_z \phi^{(bg)}(x^1, 0) = s(x^1), \quad \partial_z \bar{\phi}^{(bg)}(x^1, 0) = \bar{s}(x^1), \quad A_1^{(bg)}(x^1, 0) = a_1(x^1), \quad (\text{B.15})$$

while for the fluctuations we impose Dirichlet boundary conditions

$$\delta g_{\mu\nu}(x^1, 0) = \delta A_\mu(x^1, 0) = \delta \phi(x^1, 0) = \delta \bar{\phi}(x^1, 0) = 0. \quad (\text{B.16})$$

Again, we focus on the \mathcal{PT} -breaking phase of the non-Hermitian lattice of section 3. Hence, after fixing $LM = 6$ and $q = 1$, the solutions are characterized by two background parameters $\{a, T/M\}$ and the dimensionless momentum k/M .

As indicated in section 3.3 fluctuations can be decoupled into two sectors according to their transformation under reflections along the x^2 axis

i. Odd: $\{\delta g_{t2}, \delta g_{12}, \delta A_2\}$.

ii. Even: $\{\delta g_{tt}, \delta g_{t1}, \delta g_{11}, \delta g_{22}, \delta \phi, \delta \bar{\phi}, \delta A_t, \delta A_1\}$.

In the present discussion we consider only the even sector. We choose the following set of linearized equations for the fluctuations satisfying the requirements indicated in the previous subsection

$$\delta \mathcal{E}_{tz} = \delta \mathcal{E}_{11} = \delta \mathcal{E}_{22} = \delta \mathcal{E}_{1z} = \delta \mathcal{M}_t = \delta \mathcal{M}_1 = \delta \mathcal{F} = \delta \bar{\mathcal{F}} = 0, \quad (\text{B.17})$$

and we are left with

$$\delta \mathcal{E}_{tt} = \delta \mathcal{E}_{t1} = \delta \mathcal{E}_{zz} = \delta \mathcal{M}_z = 0, \quad (\text{B.18})$$

as the remaining unused equations. We do not present here the explicit form of these equations; instead we follow the notation used in equations (2.15) with the delta indicating that we consider the terms linear in the fluctuations. Similarly to what we found in the probe limit, the set of equations (B.17) is quadratic in ω and to have a generalized eigenvalue problem we need to include the following auxiliary fields.

$$\{\delta \tilde{g}_{11}, \delta \tilde{g}_{22}, \delta \tilde{A}_1, \delta \tilde{\phi}, \delta \tilde{\bar{\phi}}\} = -i\omega \{\delta g_{11}, \delta g_{22}, \delta A_1, \delta \phi, \delta \bar{\phi}\}. \quad (\text{B.19})$$

With this, we have properly set up the problem and we proceed with the numerics as indicated in the toy model of the previous section. We discretize the system in a lattice, compute the background solution, construct the \mathcal{Q} matrix, obtain a small set of low-lying eigenvalues and eigenvectors using Arnoldi iteration and finally select only those that satisfy the discretized version of equations (B.18) to a certain tolerance.

Regarding the background solution we proceed as described in section 3.1. The only relevant change being that now the reference background metric for the DeTurck trick is given by the SAdS₃₊₁ metric in regular coordinates

$$ds_{\text{ref}}^2 = \frac{1}{z^2} \left[-(1 - z^3)dt^2 + (dx^1)^2 + (dx^2)^2 + (1 + z^3)dz^2 - 2z^3 dt dz \right]. \quad (\text{B.20})$$

It is also worth mentioning that the ansatz (B.14) allows for non-stationary solutions [44]. We however, want to focus solely on solutions which are stationary, i.e., solutions with constant temperature. For that reason, after discretizing the problem we choose to replace two of the equations of motion at $z = 1$ by

$$h_1(x^1, 1) = h_6(x^1, 1), \quad h_7(x^1, 1) = 0. \quad (\text{B.21})$$

This imposes stationarity and fixes the temperature to be $T = 3/(4\pi)$.²⁰ For consistency, we check that the metric is regular and stationary throughout the bulk; the

²⁰The constraints (B.21) are obtained from demanding that ∂_t is the killing vector generating the event horizon at $z = 1$ corresponding to a black brane with temperature $T = 3/(4\pi)$.

Re(ω)	Im(ω)
0	-0.0471596
± 0.99668	-0.577632
± 0.996231	-0.578915
0	-1.61755
± 1.2865	-1.52129
± 2.09019	-0.466238

Table 2: QNFs for $\{a, T/M\} = \{0.4, 1\}$ at $k/M = \frac{4\pi}{3} \cdot 10^{-4}$.

latter requirement corresponding to demanding that the time-like killing vector is surface orthogonal, i.e., that numerically

$$\tilde{k}_t \wedge d\tilde{k}_t = 0, \quad (\text{B.22})$$

where

$$\tilde{k}_t = g_{t\mu} dx^\mu. \quad (\text{B.23})$$

For completeness, in table 2 we reproduce the QNFs corresponding to $\{a, T/M\} = \{0.4, 1\}$ and $k/M = \frac{4\pi}{3} \cdot 10^{-4}$. These are obtained using a lattice with $N_1 \times N_z = 16 \times 20$ sites and a tolerance of 10^{-8} . In order to locate the shown QNFs, we have obtained a total of 70 eigenvalues and eigenvectors of \mathcal{Q} . As in the probe limit, we found that it was necessary to artificially increase the numerical precision to $5 \times \text{MachinePrecision}$ when computing the eigenvalues in order to avoid spectral instability.

References

- [1] M. N. Chernodub and P. Millington, *IR/UV mixing from local similarity maps of scalar non-Hermitian field theories*, *Phys. Rev. D* **105** (2022), no. 7 076020 [[2110.05289](#)].
- [2] C. M. Bender and S. Boettcher, *Real spectra in nonHermitian Hamiltonians having PT symmetry*, *Phys. Rev. Lett.* **80** (1998) 5243–5246 [[physics/9712001](#)].
- [3] P. D. Mannheim, *Antilinearity rather than Hermiticity as a guiding principle for quantum theory*, *Journal of Physics A: Mathematical and Theoretical* **51** (jun, 2018) [[1512.04915](#)].
- [4] C. M. Bender, *Introduction to pt-symmetric quantum theory*, *Contemporary Physics* **46** (July, 2005) 277–292.
- [5] A. Mostafazadeh, *PseudoHermiticity versus PT symmetry. The necessary condition for the reality of the spectrum*, *J. Math. Phys.* **43** (2002) 205–214 [[math-ph/0107001](#)].

- [6] A. Mostafazadeh, *PseudoHermiticity versus PT symmetry 2. A Complete characterization of nonHermitian Hamiltonians with a real spectrum*, *J. Math. Phys.* **43** (2002) 2814–2816 [[math-ph/0110016](#)].
- [7] A. Mostafazadeh, *PseudoHermiticity versus PT symmetry 3: Equivalence of pseudoHermiticity and the presence of antilinear symmetries*, *J. Math. Phys.* **43** (2002) 3944–3951 [[math-ph/0203005](#)].
- [8] D. Arean, D. Garcia-Fariña and K. Landsteiner, *Strongly Coupled PT-Symmetric Models in Holography*, **11**, 2024. [2411.18471](#).
- [9] R. El-Ganainy, K. G. Makris, M. Khajavikhan, Z. H. Musslimani, S. Rotter and D. N. Christodoulides, *Non-Hermitian physics and PT symmetry*, *Nature Physics* **14** (Jan, 2018) 11–19.
- [10] Y. Ashida, S. Furukawa and M. Ueda, *Parity-time-symmetric quantum critical phenomena*, *Nature Communications* **8** (June, 2017).
- [11] C. M. Bender, D. C. Brody and H. F. Jones, *Scalar quantum field theory with a complex cubic interaction*, *Physical Review Letters* **93** (Dec., 2004).
- [12] M. N. Chernodub and P. Millington, *Anomalous dispersion, superluminality, and instabilities in two-flavor theories with local non-Hermitian mass mixing*, *Phys. Rev. D* **109** (2024), no. 10 105006 [[2401.06097](#)].
- [13] J. M. Maldacena, *The Large N limit of superconformal field theories and supergravity*, *Adv. Theor. Math. Phys.* **2** (1998) 231–252 [[hep-th/9711200](#)].
- [14] O. Aharony, S. S. Gubser, J. M. Maldacena, H. Ooguri and Y. Oz, *Large N field theories, string theory and gravity*, *Phys. Rept.* **323** (2000) 183–386 [[hep-th/9905111](#)].
- [15] M. Ammon and J. Erdmenger, *Gauge/gravity duality: Foundations and applications*. Cambridge University Press, Cambridge, 4, 2015.
- [16] J. Zaanen, Y. Liu, Y. Sun and K. Schalm, *Holographic Duality in Condensed Matter Physics*. Cambridge University Press, 2015.
- [17] S. A. Hartnoll, A. Lucas and S. Sachdev, *Holographic Quantum Matter*. MIT Press, 2018.
- [18] D. Areán, K. Landsteiner and I. Salazar Landea, *Non-hermitian holography*, *SciPost Phys.* **9** (2020), no. 3 032 [[1912.06647](#)].
- [19] Z.-Y. Xian, D. Rodríguez Fernández, Z. Chen, Y. Liu and R. Meyer, *Electric conductivity in non-Hermitian holography*, *SciPost Phys.* **16** (2024) 004 [[2304.11183](#)].
- [20] S. Morales-Tejera and K. Landsteiner, *Non-Hermitian quantum quenches in holography*, *SciPost Phys.* **14** (2023), no. 3 030 [[2203.02524](#)].
- [21] W. Cai, S. Cao, X.-H. Ge, M. Matsumoto and S.-J. Sin, *Non-Hermitian quantum*

- system generated from two coupled Sachdev-Ye-Kitaev models, *Phys. Rev. D* **106** (2022), no. 10 106010 [[2208.10800](#)].
- [22] S. Cao and X.-H. Ge, *Excitation Transmission through a non-Hermitian traversable wormhole*, [2404.11436](#).
- [23] D. Z. Freedman, S. S. Gubser, K. Pilch and N. P. Warner, *Renormalization group flows from holography supersymmetry and a c theorem*, *Adv. Theor. Math. Phys.* **3** (1999) 363–417 [[hep-th/9904017](#)].
- [24] R. C. Myers and A. Sinha, *Seeing a c-theorem with holography*, *Phys. Rev. D* **82** (2010) 046006 [[1006.1263](#)].
- [25] R. C. Myers and A. Sinha, *Holographic c-theorems in arbitrary dimensions*, *JHEP* **01** (2011) 125 [[1011.5819](#)].
- [26] A. Donos and S. A. Hartnoll, *Interaction-driven localization in holography*, *Nature Phys.* **9** (2013) 649–655 [[1212.2998](#)].
- [27] A. Donos and J. P. Gauntlett, *Novel metals and insulators from holography*, *JHEP* **06** (2014) 007 [[1401.5077](#)].
- [28] A. Donos and J. P. Gauntlett, *The thermoelectric properties of inhomogeneous holographic lattices*, *JHEP* **01** (2015) 035 [[1409.6875](#)].
- [29] S. A. Hartnoll, D. M. Ramirez and J. E. Santos, *Emergent scale invariance of disordered horizons*, *JHEP* **09** (2015) 160 [[1504.03324](#)].
- [30] M. Headrick, S. Kitchen and T. Wiseman, *A New approach to static numerical relativity, and its application to Kaluza-Klein black holes*, *Class. Quant. Grav.* **27** (2010) 035002 [[0905.1822](#)].
- [31] G. T. Horowitz, J. E. Santos and D. Tong, *Optical Conductivity with Holographic Lattices*, *JHEP* **07** (2012) 168 [[1204.0519](#)].
- [32] O. J. C. Dias, J. E. Santos and B. Way, *Numerical Methods for Finding Stationary Gravitational Solutions*, *Class. Quant. Grav.* **33** (2016), no. 13 133001 [[1510.02804](#)].
- [33] S. S. Gubser and A. Nellore, *Ground states of holographic superconductors*, *Phys. Rev. D* **80** (2009) 105007 [[0908.1972](#)].
- [34] S. A. Hartnoll and J. E. Santos, *Disordered horizons: Holography of randomly disordered fixed points*, *Phys. Rev. Lett.* **112** (Jun, 2014) 231601.
- [35] K. Skenderis, *Lecture notes on holographic renormalization*, *Classical and Quantum Gravity* **19** (Nov., 2002) 5849–5876.
- [36] S. A. Hartnoll, C. P. Herzog and G. T. Horowitz, *Holographic superconductors*, *Journal of High Energy Physics* **2008** (Dec., 2008) 015–015.
- [37] P. Yang, X. Li and Y. Tian, *Instability of holographic superfluids in optical lattice*, *JHEP* **11** (2021) 190 [[2109.09080](#)].
- [38] L. N. Trefethen and M. Embree, *Spectra and Pseudospectra: The Behavior of Nonnormal Matrices and Operators*. Princeton University Press, 2005.

- [39] C. M. Warnick, *On quasinormal modes of asymptotically anti-de Sitter black holes*, *Commun. Math. Phys.* **333** (2015), no. 2 959–1035 [[1306.5760](#)].
- [40] D. Areán, D. Garcia-Fariña and K. Landsteiner, *Pseudospectra of holographic quasinormal modes*, *JHEP* **12** (2023) 187 [[2307.08751](#)].
- [41] P. Bizoń, T. Chmaj and P. Mach, *A toy model of hyperboloidal approach to quasinormal modes*, *Acta Phys. Polon. B* **51** (2020) 1007 [[2002.01770](#)].
- [42] R. Panosso Macedo, *Hyperboloidal approach for static spherically symmetric spacetimes: a didactical introduction and applications in black-hole physics*, [2307.15735](#).
- [43] R. Panosso Macedo and A. Zenginoglu, *Hyperboloidal Approach to Quasinormal Modes*, [2409.11478](#).
- [44] P. Figueras and T. Wiseman, *Stationary holographic plasma quenches and numerical methods for non-Killing horizons*, *Phys. Rev. Lett.* **110** (2013) 171602 [[1212.4498](#)].